EXPERIMENTAL AND SIMULATION STUDIES OF

SEQUESTRATION OF SUPERCRITICAL CARBON DIOXIDE IN

DEPLETED GAS RESERVOIRS

A Dissertation

by

JEONG GYU SEO

Submitted to the Office of Graduate Studies of
Texas A&M University
in partial fulfillment of the requirements for the degree of

DOCTOR OF PHILOSOPHY

May 2004

Major Subject: Petroleum Engineering

EXPERIMENTAL AND SIMULATION STUDIES OF

SEQUESTRATION OF SUPERCRITICAL CARBON DIOXIDE IN

DEPLETED GAS RESERVOIRS

A Dissertation

by

JEONG GYU SEO

Submitted to the Office of Graduate Studies of
Texas A&M University
in partial fulfillment of the requirements for the degree of

DOCTOR OF PHILOSOPHY

Approved as to style and content by:

_____	_____
Daulat D. Mamora	David S. Schechter
(Co-Chair of Committee)	(Co-Chair of Committee)
_____	_____
Thomas A. Blasingame	Luc T. Ikelle
(Member)	(Member)
_____	
Stephen A. Holdich	
(Head of Department)	

May 2004

Major Subject: Petroleum Engineering

ABSTRACT

Experimental and Simulation Studies of Sequestration of Supercritical Carbon Dioxide

in Depleted Gas Reservoirs. (May 2004)

Jeong Gyu Seo, B.S., Hanyang University, Korea;

M.S., Hanyang University, Korea

Co-Chairs of Advisory Committee: Dr. Daulat D. Mamora
Dr. David S. Schechter

Experimental, analytical, and simulation studies have been conducted to evaluate the feasibility of sequestering supercritical CO_2 in depleted gas reservoirs. The experimental runs involved the following steps. First, the 1 ft long by 1 in. diameter carbonate core is inserted into a viton Hassler sleeve and placed inside an aluminum coreholder that is then evacuated. Second, with or without connate water, the carbonate core is saturated with methane. Third, supercritical CO_2 is injected into the core with 300 psi overburden pressure. From the volume and composition of the produced gas measured by a wet test meter and a gas chromatograph, the recovery of methane at CO_2 breakthrough is determined. The core is scanned three times during an experimental run to determine core porosity and fluid saturation profile: at start of the run, at CO_2 breakthrough, and at the end of the run. Runs were made with various temperatures, 20°C (68°F) to 80°C (176°F), while the cell pressure is varied, from 500 psig (3.55 MPa) to 3000 psig (20.79 MPa) for each temperature.

An analytical study of the experimental results has been also conducted to determine

the dispersion coefficient of CO_2 using the convection-dispersion equation. The dispersion coefficient of CO_2 in methane is found to be relatively low, 0.01-0.3 cm^2/min.

Based on experimental and analytical results, a 3D simulation model of one eighth of a 5-spot pattern was constructed to evaluate injection of supercritical CO_2 under typical field conditions. The depleted gas reservoir is repressurized by CO_2 injection from 500 psi to its initial pressure 3,045 psi. Simulation results for 400 bbl/d CO_2 injection may be summarized as follows. First, a large amount of CO_2 is sequestered: (i) about 1.2 million tons in 29 years (0 % initial water saturation) to 0.78 million tons in 19 years (35 % initial water saturation) for 40-acre pattern, (ii) about 4.8 million tons in 112 years (0 % initial water saturation) to 3.1 million tons in 73 years (35 % initial water saturation) for 80-acre pattern. Second, a significant amount of natural gas is also produced: (i) about 1.2 BSCF or 74 % remaining GIP (0 % initial water saturation) to 0.78 BSCF or 66 % remaining GIP (35 % initial water saturation) for 40-acre pattern, (ii) about 4.5 BSCF or 64 % remaining GIP (0 % initial water saturation) to 2.97 BSCF or 62 % remaining GIP (35 % initial water saturation) for 80-acre pattern. This produced gas revenue could help defray the cost of CO_2 sequestration. In short, CO_2 sequestration in depleted gas reservoirs appears to be a win-win technology.

DEDICATION

My graduate studies at Texas A&M University would not have been possible without the support and understanding of my wife and son. This dissertation is dedicated to:

my wife,   *Eunsun Lee,*

my son: *Eric Hyobin Seo,*

and

to my parents, my father Soobeom Seo, my mother Dongsil Cho, and my grandmother

for their support, love, prayer, and guidance.

ACKNOWLEDGEMENTS

TABLE OF CONTENTS

LIST OF TABLES

LIST OF FIGURES

FIGURE   Page

FIGURE   Page

CHAPTER I

INTRODUCTION

CO_2 emission from burning fossil fuels has been identified as the major contributor to the increase in atmospheric CO_2 levels that can potentially lead to global climate change. In the last decade, there has been worldwide concern on possible global warming caused by heat being trapped by CO_2 in the upper atmosphere (the green-house effect).

Carbon dioxide sequestration can be defined as the capture and secure storage of carbon dioxide that would otherwise be emitted to or remain in the atmosphere. The idea is (1) to keep carbon dioxide emissions produced by human activities from reaching the atmosphere by capturing and diverting them to secure storage, or (2) to remove carbon dioxide from the atmosphere by various means and store it.

It is important to carry out research on carbon dioxide sequestration for several reasons:[1]

- Carbon dioxide sequestration could be a major tool for reducing carbon dioxide emissions from fossil fuels.

    However, much work remains to be done to understand the science and engineering aspects and potential of carbon dioxide sequestration.

This dissertation follows the style and format of the *Journal of Petroleum Technology.*

- Given the magnitude of carbon dioxide emission reductions needed to stabilize the atmospheric CO_2 concentration, multiple approaches to carbon dioxide management will be needed.

- Carbon dioxide sequestration is compatible with the continued large-scale use of fossil fuels, as well as greatly reduced emissions of CO_2 to the atmosphere. Current estimates of fossil fuel resources – including conventional oil and gas, coal, and unconventional fossil fuels such as heavy oil and tar sands – imply sufficient resources to supply a very large fraction of the world's energy sources through the next century.

One set of options involves capturing carbon dioxide from fossil fuel use before it reaches the atmosphere. For example, CO_2 could be separated from power plant flue gases, from effluents of industrial process (e.g., in oil refineries and iron, steel, and cement production plants), or during production of decarbonized fuels (such as hydrogen produced from hydrocarbons such as natural gas or coal). The captured CO_2 could be concentrated into a liquid or gas stream that could be transported and injected into the oil and gas reservoirs, the ocean, deep saline aquifers, and deep coal seams and beds (**Fig. 1.1**).
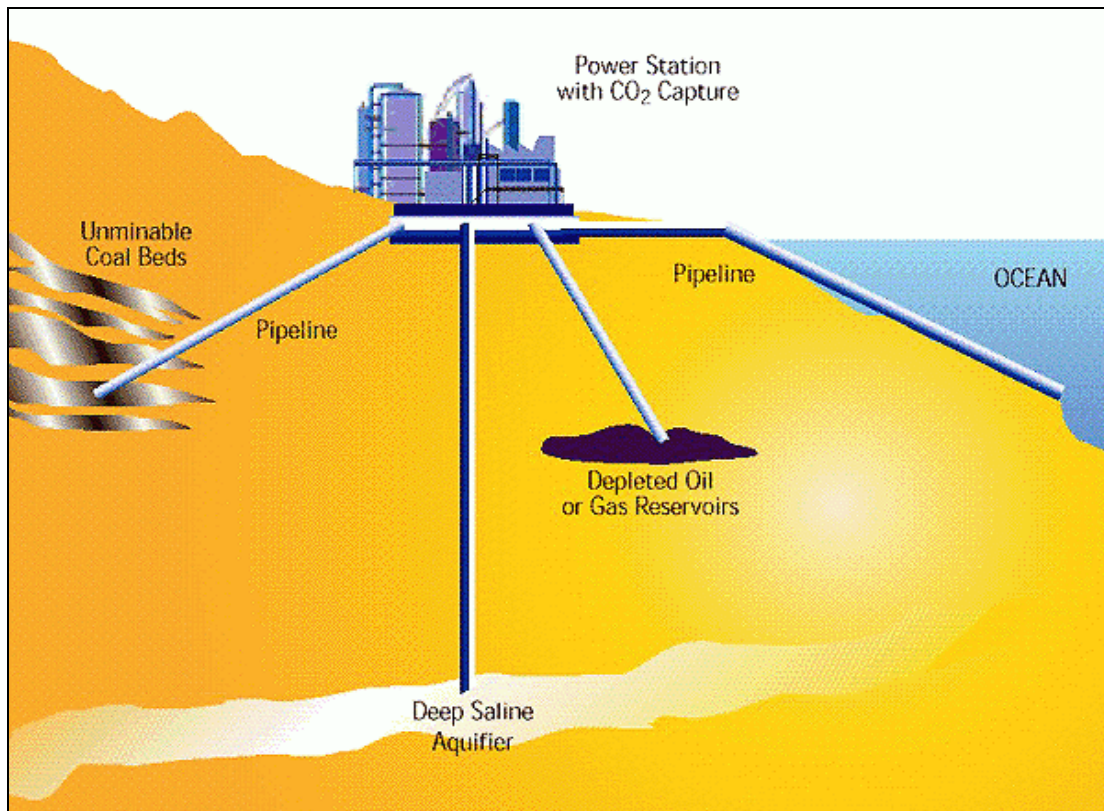
Fig. 1.1 – Storage sites for carbon dioxide in the ground and deep sea (IEA Greenhouse Gas R&D Programme). [2]

In general, storage sites for carbon dioxide can be divided into two categories: geological sites and marine sites. Some of the advantages and disadvantages are summarized in Table 1.1.[3,4]

TABLE 1.1 – GEOLOGICAL AND MARINE SEQUESTRATION OPTIONS: ADVANTAGES AND DISADVANTAGES

Geological Sites	Advantages	Disadvantages
Coal beds	Large capacity	High costs
Mined salt domes	Custom designs	High costs
Deep saline aquifers	Large capacity	Unknown storage integrity
Depleted oil or gas reservoirs	Proven storage integrity	Limited capacity
Marine Sites	Advantages	Disadvantages
Droplet plume	Minimal environmental effects	Some leakage
Towed pipe	Minimal environmental effects	Some leakage
Dry ice	Simply technology	High costs
Carbon dioxide lake	Carbon dioxide will remain in ocean for thousands of years	Immature technology

Stevens et $al.$[5] provide estimates of CO_2 sequestration potential of selected worldwide coal basins for application of CO_2-Enhanced Coal Bed Methane (ECBM) technology and suggest that large potential for CO_2 sequestration exists. But CO_2-

ECBM is presently not commercial due to the high cost of capture, compression and transportation of the CO_2. Advancement in CO_2-ECBM technology, reduced costs, higher natural gas prices, and government-imposed credits would improve the economics of sequestration in coal beds.

The technology of fluid storage in mined salt domes has already been developed and applied for underground storage of petroleum, natural gas and compressed air or for salt mining for public and industrial use.[6,7,8] Currently, single salt caverns are up to 5×10^5 m^3 in volume and can store fluids at pressures up to 80% of the fracturing threshold. Although salt and rock caverns theoretically have a large storage capacity, the associated costs are too high, and the environmental problems relating to rock and brine disposal are significant.[9]

Saline aquifers are attractive as CO_2 disposal reservoirs because they are generally unused and are available in many parts of the U.S. However, it is important to investigate the behavior of CO_2 injected into aquifers for effective and safe CO_2 storage. In particular, CO_2 injected into aquifers might cause a problem like CO_2 hydrate formation.[10]

CO_2 injection into oil and gas reservoirs can provide collateral benefits in terms of enhancing recovery of oil and natural gas.[11]

1.1 Background

In the past 60 years, the amount of anthropogenic carbon dioxide (CO_2) emitted to the atmosphere, primarily because of expanding use of fossil fuels for energy, has risen from preindustrial levels of 280 parts per million (ppm) to present levels of over 365 ppm.[1]   Predictions of global energy use in the next century suggest a continued increase in carbon emissions and rising concentrations of CO_2 in the atmosphere unless major changes are made in the way we produce and use energy – in particular, how we manage carbon.

In 1996 the Norwegian state oil company, Statoil, started the first large-scale underground disposal of CO_2 in the North Sea.[12,13]   Some 1 million tonnes per year of CO_2 - separated out of the natural gas produced from the Sleipner Vest field - has been injected into the overlying Utsira aquifer. A similar project is being planned for the Natuna gas field in Indonesia. The field contains some 1.4×10^6 m^3 (50 TSCF) gas, about 70% by volume of which is carbon dioxide. The Natuna project, to be undertaken by a consortium of companies, would involve liquefying the sales gas (LNG) while the carbon dioxide would be injected into an aquifer.

Underground disposal of CO_2 emitted by industrial sources such as fossil fuel-fired power plants has not been undertaken. In the last decade, however, there has been worldwide concern on possible global warming caused by heat being trapped by CO_2 in the upper atmosphere (the green-house effect). In 1993, the European Commission began the Joule II Non-nuclear Energy Research Program, which studied sequestration of industrially produced CO_2.[13,14]

The Joule II study concluded that (i) shallow reservoirs do not provide sufficient storage for carbon dioxide because it would be in gaseous form, (ii) for maximum storage capacity, carbon dioxide has to be stored as a supercritical fluid - which requires reservoirs deeper than 800 m (2,600 ft), (iii) such deep reservoirs could be depleted oil or gas reservoirs or structures containing aquifers, (iv) if carbon dioxide is stored in aquifers, then to avoid contaminating shallower potable water sources, carbon dioxide would be sequestered in aquifers deep below the North Sea, (v) if carbon dioxide is injected into a limestone reservoir, carbonate dissolution could occur around the injection wells causing subsidence, and (vi) the cost of carbon dioxide separation out of flue gas is significantly higher than that of transporting and injecting carbon dioxide in reservoirs.

As part of the Joule II project, Pearce *et al.* (1996)[15] conducted hydrothermal experiments to determine the effect of carbon dioxide (as supercritical fluid or saturated in water) on anhydrites, mudstones, and sandstones. These experiments were restricted to observation of changes to the physical properties and chemical composition of the rocks after carbon dioxide was passed through the rock samples. Reaction kinetic parameters were not measured. Excluded from the study were carbonate rocks – these would have been more reactive to carbon dioxide.

Carbon dioxide sequestration is a very recent development. Uncertainties still exist with respect to the process of injecting carbon dioxide into depleted gas reservoirs.

1.2 Research Objectives

The main objectives of the research are as follows.

1. Determine the coefficient of dispersion of supercritical carbon dioxide in gas-bearing carbonate reservoirs.

2. Understand and model the displacement of natural gas by supercritical CO_2 in a depleted carbonate porous medium.

3. Determine gas-liquid relative permeability curves to be used in the field simulation study.

4. Evaluate injection of supercritical CO_2 under typical field conditions.

Experimental and simulation study were conducted with the objective of better understanding the feasibility of sequestering supercritical CO_2 in depleted gas reservoirs.

1.3 Organization of Dissertation

A literature review of natural gas storage in the U.S., enhanced coalbed methane recovery using carbon dioxide, sequestration of supercritical carbon dioxide in depleted gas fields, supercritical conditions, dispersion coefficient, and model studies using the X-ray CT scanner is given in Chapter II.   A description of the experimental apparatus and procedure used in this study is given in Chapter III.   The results of the experiments are presented in Chapter IV.   A simulation study to evaluate injection of supercritical CO_2 under typical field conditions is given in Chapter V.   Discussion on the results of the experimental and simulation study is given in Chapter VI.

CHAPTER II

LITERATURE REVIEW

To gain further insight into the process of CO_2 sequestration in depleted gas reservoirs, we have reviewed literature on two somewhat similar processes, namely, the storage of natural gas in the U.S., and enhanced coalbed methane (ECBM) recovery using carbon dioxide injection. We have also reviewed literature on the following sequestration of supercritical carbon dioxide in depleted gas fields, supercritical conditions, dispersion coefficient, and model studies using the x-ray CT scanner to measure fluid and rock parameters in displacement of methane by supercritical carbon dioxide.

2.1 Natural Gas Storage in the U.S.

The process of storing piped natural gas in depleted gas reservoirs in summer, and subsequently producing the gas in winter, began in the U.S. in 1915.[16,17] Since then, the underground gas storage industry in the U.S. has developed into a mature industry. By 1979, about 211×10^9 m^3 (7.437 TSCF) of natural gas was stored in 399 reservoirs in 26 states with seasonal gas withdrawal of 1.1×10^9 m^3 (39.7 BSCF). About 80% of the storage capacity was provided by *depleted gas reservoirs* and 20% by injecting natural gas into aquifer-filled structures. Storage reservoir pressures ranged from 2.07 to 27.6 Mpa (300 to 4,000 psi).

A depleted natural gas reservoir (containing mainly methane) can store significantly more gas than a depleted oil reservoir, presuming that each reservoir has the same initial hydrocarbon pore volume. This is due to two reasons. First, ultimate gas recovery (typically about 65% of initial gas-in-place) is about twice that of oil (average 35% of initial oil-in-place). Also, gas density (e.g., an average in-situ gradient about 1.81 kPa/m (0.08 psi/ft)) is significantly less than that of oil, which is typically about 6.11 kPa/m (0.27 psi/ft). There is therefore less remaining hydrocarbon mass in a gas reservoir than in an oil reservoir. Secondly, gas is some 30 times more compressible than oil or water. At 13.8 MPa (2000 psia), isothermal compressibility of natural gas is typically about 72.5×10^{-6} kPa^{-1} (500×10^{-6} psi^{-1}) versus 2.2×10^{-6} kPa^{-1} (15×10^{-6} psi^{-1}) for oil and 0.4×10^{-6} kPa^{-1} (3×10^{-6} psi^{-1}) for water. As borne out by natural gas storage in the U.S., a depleted gas reservoir would appear to be best suited for carbon dioxide sequestration.

We then evaluated the possible gain in producing additional natural gas resulting from gas reservoirs being re-pressurized by carbon dioxide injection. Using the 1979 AGA data, the average storage capacity per reservoir for the 399 gas storage depleted reservoirs is 0.53×10^9 m^3 (18.64 BSCF). Making a conservative assumption that this volume is equal to the initial gas-in-place volume per reservoir, and a recovery factor of 65%, the hitherto unrecoverable gas reserves amount to about $0.35 \times 0.53 \times 10^9$ m^3, i.e. 0.19×10^9 m^3 (6.52 BSCF). If carbon dioxide were injected into such a reservoir, re-pressurizing it and displacing the natural gas, the potential value of the gas could be as high as $12 million, assuming a gas price of $1.90/MSCF (6.71 cents/m^3). For a reservoir with, say, ten times larger initial gas-in-place or where ten of such reservoirs

are in close proximity to one another and therefore be treated as a single carbon dioxide sequestration point, then the potential value of the produced gas (1.9×10^9 m^3 or 65.2 BSCF) could be as high as \$120 million.   These gas revenues could be used to offset the costs of carbon dioxide transportation, injection wells, etc.   Further, the production of natural gas has the benefit of providing additional storage space for carbon dioxide.

2.2 Enhanced Coalbed Methane Recovery Using Carbon Dioxide

Methane is conventionally produced from coal seams by pressure depletion that causes methane to desorb from the coalbed.   Injected carbon dioxide is preferentially adsorbed by coal causing desorption and thus production of methane.   In 1995, Burlington Resources commenced carbon dioxide injection into the Allison Unit coalbed in the San Juan Basin, New Mexico, to enhance coalbed methane recovery.[18]   This world's first CO_2 enhanced coalbed methane (CO_2-ECBM) pilot consisted of a 4-injector/7-producer pattern. CO_2 was supplied from a nearby pipeline that transports the gas at 13.8 MPa (2000 psi) from a carbon dioxide field in Colorado for injection into oil fields in West Texas to enhance oil recovery.

Some 85×10^3 m^3/D (3 MMSCF/D) of carbon dioxide was injected, with gas production enhanced by up to 150% over the conventional pressure-depletion method. As of 1998, more than 57×10^6 m^3 (2 BSCF) carbon dioxide has been sequestered at the Allison pilot project.   Pilot results indicate CO_2-ECBM would be profitable in the San Juan Basin at wellhead gas prices above 6.18 cents/m^3 (\$1.75/MSCF), possibly adding

as much as 3.7×10^{11} m^3 (13 TSCF) methane production – a resource value of \$22.8 billion.

Coalbed methane development in the San Juan basin accounts for 75% of world coalbed methane production. Stevens and Riemer (1998)[17] also estimated that possible commercial CO_2-ECBM worldwide could be as high as 1.93×10^{12} m^3 (68 TSCF) with about 7.1 billion metric tonnes carbon dioxide sequestration potential.

2.3 Sequestration of Supercritical Carbon Dioxide in Depleted Gas Fields

Carbon dioxide has a critical temperature of 31°C (88°F) and a critical pressure of 7.38 MPa (1070 psia). Thus, at pressures and temperatures typically encountered in the field, CO_2 will behave as a supercritical fluid. CO_2 in this form is transported via surface pipelines from states such as New Mexico to West Texas for injection into oil reservoirs to enhance oil recovery.[19] However, displacement of natural gas in a reservoir by supercritical CO_2 has not been done because there has been no compelling reason to do so except for injection of CO_2 to enhance coalbed methane production.

2.4 Supercritical Conditions

Carbon dioxide will behave as a supercritical fluid at pressures and temperatures typically encountered in the field. Supercritical fluids have liquid-like densities, gas-like diffusivities and could be liquid or gas dependent on pressure and temperature change in the field.[20]

The term "supercritical condition" - although often used - is not well-defined.   For instance, the term is not used or defined in standard references such as Katz *et al*.'s "*Handbook of Natural Gas Engineering*", or McCain's "*The Properties of Petroleum Fluids*".   We have used the term in a conservative manner, i.e. "supercritical condition" refers to the region in the PT diagram where <u>both</u> $P > P_{\text{critical}}$ and $T > T_{\text{critical}}$ are satisfied. Carbon dioxide has a critical temperature of 31°C (88°F) and a critical pressure of 7.38 MPa (1,070 psia).   For methane, the critical temperature is $-$ 82.8°C (-117°F) and the critical pressure is 4.64 MPa (673 psia).

2.5 Dispersion Coefficient

Mixing of fluids in porous media during a displacement is a diffusion-like process. The dispersion coefficient depends on the direction of the dispersion flux with respect to the main convective flux.   The largest value occurs for dispersion in the main flow direction (longitudinal dispersion), and the smallest value occurs for dispersion perpendicular to the main flow direction (transversal dispersion).[21]

The following convection-dispersion-reaction equation describes the overall transport and reaction of carbon dioxide for one-dimensional flow.

$$K_l \frac{\partial^2 C}{\partial x^2} - v \frac{\partial C}{\partial x} - C_R = \frac{\partial C}{\partial t} \quad \text{…………………………………………..} \quad (2.1)$$

where C is concentration of supercritical carbon dioxide at time t and location x, C_R is reaction rate concentration of supercritical carbon dioxide with the reservoir, K_l is

coefficient of longitudinal dispersion, and v is interstitial velocity of supercritical carbon dioxide. If the kinetic reaction term in Eq. 2.1 is removed, we obtain the well-known convection-dispersion equation as given by Eq. 2.2.

$$K_l \frac{\partial^2 C}{\partial x^2} - v \frac{\partial C}{\partial x} = \frac{\partial C}{\partial t} \qquad \text{...} \quad (2.2)$$

Eq. 2.2 may be expressed in dimensionless form as follows.

$$\frac{1}{P_e} \frac{\partial^2 C}{\partial x_D{}^2} - \frac{\partial C}{\partial x_D} = \frac{\partial C}{\partial t_D} \qquad \text{..} \quad (2.3)$$

where:

$x_D = \dfrac{x}{L}$,   dimensionless distance, where L is length of core,

$t_D = \dfrac{tv}{L}$,   dimensionless time, and

v,   interstitial velocity $(= Q / \pi\ r^2 \phi)$

$P_e = \dfrac{vL}{K_l}$,   Peclet number (ratio of convection to dispersion).

K_l,   Longitudinal dispersion coefficient

Since the carbon dioxide injection inlet is at $x = 0$, then

initial condition: $C = 0$ at $t_D = 0,\ 0 < x_D < \infty$

boundary conditions: $C = 1$ at $x_D = 0$

$$\left. \begin{array}{l} \\ \\ \\ C \rightarrow 0 \;\; at \;\; x_D \rightarrow \infty \end{array} \right\} \quad t_D > 0$$

Solution to Eq. 2.3 may be shown to be as follows.

$$C = \frac{1}{2}\left\{ \mathrm{erfc}\left(\frac{x_D - t_D}{2\sqrt{t_D / P_e}} \right) + e^{P_e x_D}\, \mathrm{erfc}\left(\frac{x_D + t_D}{2\sqrt{t_D / P_e}} \right) \right\} \qquad \dots\dots\dots\dots\dots\dots\dots\dots\dots \quad (2.4)$$

A computer program was written to calculate carbon dioxide concentration using Eq. 2.4 in which the dispersion coefficient K_l is varied to yield the best agreement between data and the analytical solution. In the program, erfc *(x)* is calculated using the following expression that yields an error of only 10^{-9}.[22]

$$\mathrm{erfc}(x) = (a_1 z + a_2 z^2 + a_3 z^3 + a_4 z^4 + a_5 z^5)e^{-x^2} \qquad \dots\dots\dots\dots\dots\dots\dots\dots\dots\dots \quad (2.5)$$

where:

$$z = \frac{1}{1 + 0.3275911\ x}$$

$a_1 = 0.254829592, \quad a_2 = -0.284496736, \quad a_3 = 1.421413741$

$a_4 = -1.453152027, \quad a_5 = 1.061405429$

Carbon dioxide concentration profiles are compared against those based on the analytical solution (Eq. 2.4) for various values of the dispersion coefficient. The correct dispersion coefficient would be that which gives the best agreement between data and the analytical solution.[23]

2.6 Model Studies Using X-ray CT Scanner

The petroleum industry is increasingly interested in accurate determination of reservoir rock property and fluid flow visualization. The CT scanner has been widely applied in petrophysics including three-dimensional (3D) measurement of rock density and porosity, rock mechanics studies, correlation of core logs with well logs, characterization of mud invasion, fractures, disturbed cores, quantification of complex mineralogies, and sand/shale ratios. Reservoir engineering applications include fundamental studies of CO_2 displacement in cores, focusing on viscous fingering, gravity segregation, miscibility, and mobility control.[24,25]

The x-ray computed tomography (CT) scanner was developed by Godfrey Hounsfield and Allen Cormack during the early 1970's and resulted in their receiving the Nobel Prize in 1979. The objective of the x-ray computed tomography process, or CT scanning, is to obtain descriptive images of density variations within an object in cross-sectional slices. This non-destructive evaluation process is invaluable to research in the petroleum industry by imaging fluid flow in porous media.[26,27,28]

A brief description of the principle of the CT scanner follows. Applying Beer's law, consider x-ray radiography that view an object from only one angle so that shadows from all irradiated matter along a ray path are superimposed on one another (**Fig. 2.1**).
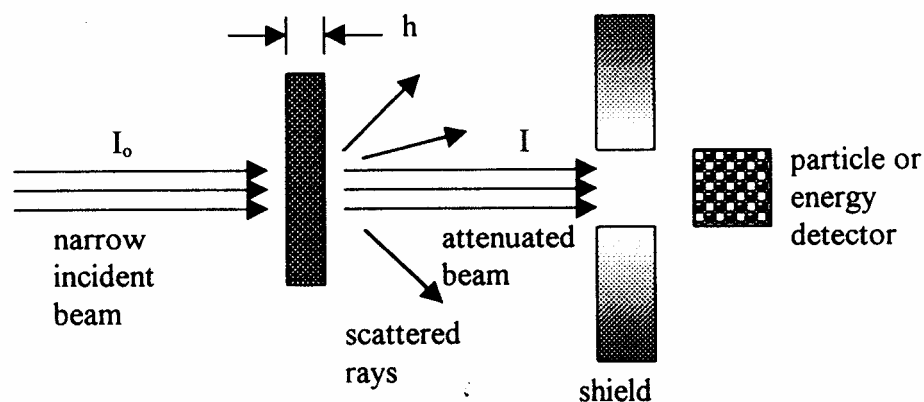
Fig. 2.1 – Application of Beer's law in x-ray radiography (after Wellington *et al.*[23]).

The basic quantity measured in each pixel of a CT image is the linear attenuation coefficient, μ. This is defined from Beer's law:[29]

$$I = I_0 e^{-\mu h} \quad \dots\dots\dots\dots\dots\dots\dots\dots\dots\dots\dots\dots\dots\dots\dots\dots\dots\dots\dots\dots\dots \quad (2.6)$$

where I_0 is the incident X-ray intensity and I is the intensity remaining after the X-ray passes through a thickness, h, of sample (**Fig. 2.1**). Beer's law assumes a well-collimated beam and a monochromatic source of X-rays.

The linear attenuation coefficient, μ, depends on both electron density (bulk density), ρ, and atomic number, Z, in the form

$$\mu = \rho\left(a + bZ^{3.8} / E^{3.2}\right) \quad \dots\dots\dots\dots\dots\dots\dots\dots\dots\dots\dots\dots\dots\dots\dots\dots\dots\dots \quad (2.7)$$

where a is a nearly energy-independent coefficient called the Klein-Nishina coefficient, b is a constant (9.8×10^{-24}), and E is the energy of the probing x-rays.[24,28,30] The first term in Eq. 2.2 represents Compton scattering, which is predominant at X-ray energies (above 100 kV) where medical CT scanners normally operate. The second term of Eq. 2.2 accounts for photoelectric absorption, which is more important at X-ray energies well below 100 kV.

The equations used to measure the porosity and saturation are as follows.[31]

$$\phi_{x,y} = \frac{CT_{x,y}^{100\% \, water} - CT_{x,y}^{dry}}{CT_{water} + 1000} \quad \dots\dots\dots\dots\dots\dots\dots\dots\dots\dots\dots\dots\dots\dots\dots\dots\dots \quad (2.8)$$

where:

$CT_{x,y}^{100\% \, Water}$ is CT number of core saturated with 100 % water at x, y position.

$CT_{x,y}^{dry}$ is CT number of dry core at x, y position.

CT_{water} is CT number of water used to calculate $CT_{x,y}^{100\% Water}$.

$$S_{x,y}^{CO_2} = \frac{CT_{x,y}^{CO_2} - CT_{x,y}^{dry}}{\phi_{x,y}\left(CT_{CO_2} + 1000\right)} \quad \dots\dots\dots\dots\dots\dots\dots\dots\dots\dots\dots\dots\dots\dots\dots\dots\dots\dots\dots \quad (2.9)$$

where:

$CT_{x,y}^{CO_2}$ is CT number of core saturated with CO_2 at x, y position.

$CT_{x,y}^{dry}$ is CT number of dry core at x, y position.

CT_{CO_2} is CT number of CO_2 used to calculate $CT_{x,y}^{100\% CO_2}$. CT_{CO_2} is estimated from

the CT number versus density plot (**Fig. 2.2**) where ρ_{CO_2} is taken as 0.56 g/cc, thus

giving CT_{CO_2} of -440 (2,700 psig, 80 °C).

$\phi_{x,y}$ is porosity at x, y position.

$y = 0.001x + 1$

◆ Run 29 (2,700 psig, 80 C)
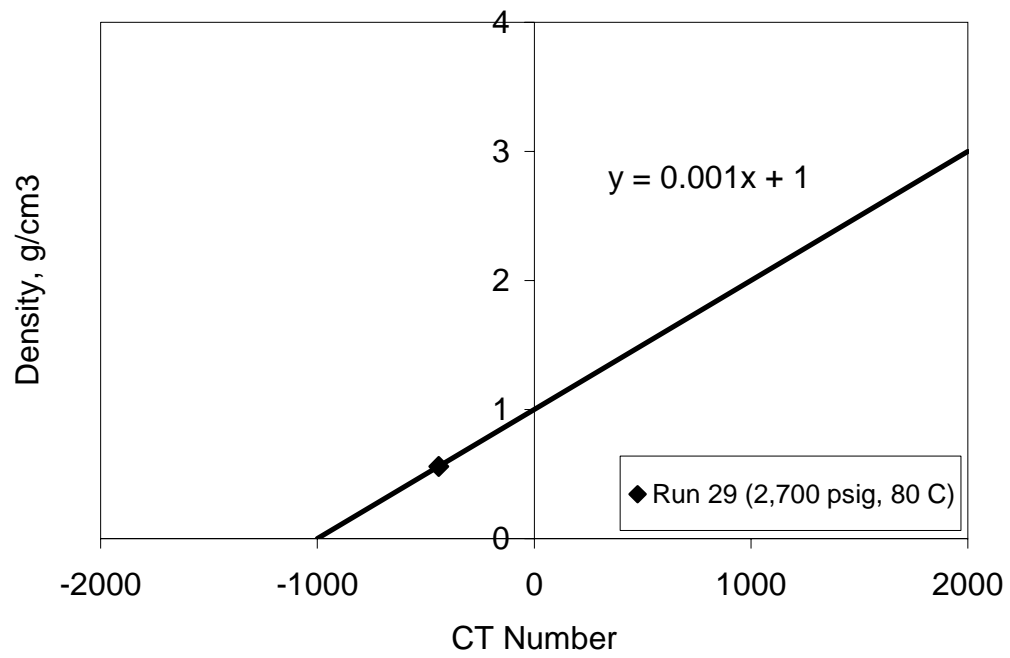
Fig. 2.2 – Calibration curve of CT number vs. density.

CHAPTER III

EXPERIMENTAL APPARATUS AND PROCEDURE

3.1 Experimental Apparatus

The experimental apparatus consists of five main components, the injection system, coreflood cell, x-ray CT scanner, production system, and data recording system (**Fig. 3.1**).   All of the apparatus used in these experiments, including the CT scanner, were available in the Department of Petroleum Engineering at Texas A&M University. However, as described later, the coreflood cell was specially designed and fabricated for the study.   **Table 3.1** lists the equipment used.   A brief description of each of these main components follows.

3.1.1 Injection System

The injection system consists of two sets of one-liter and two liter *Temco* accumulator connected to a *ISCO* syringe water pump, one set for each of the gases, methane and carbon dioxide (**Fig. 3.2**).
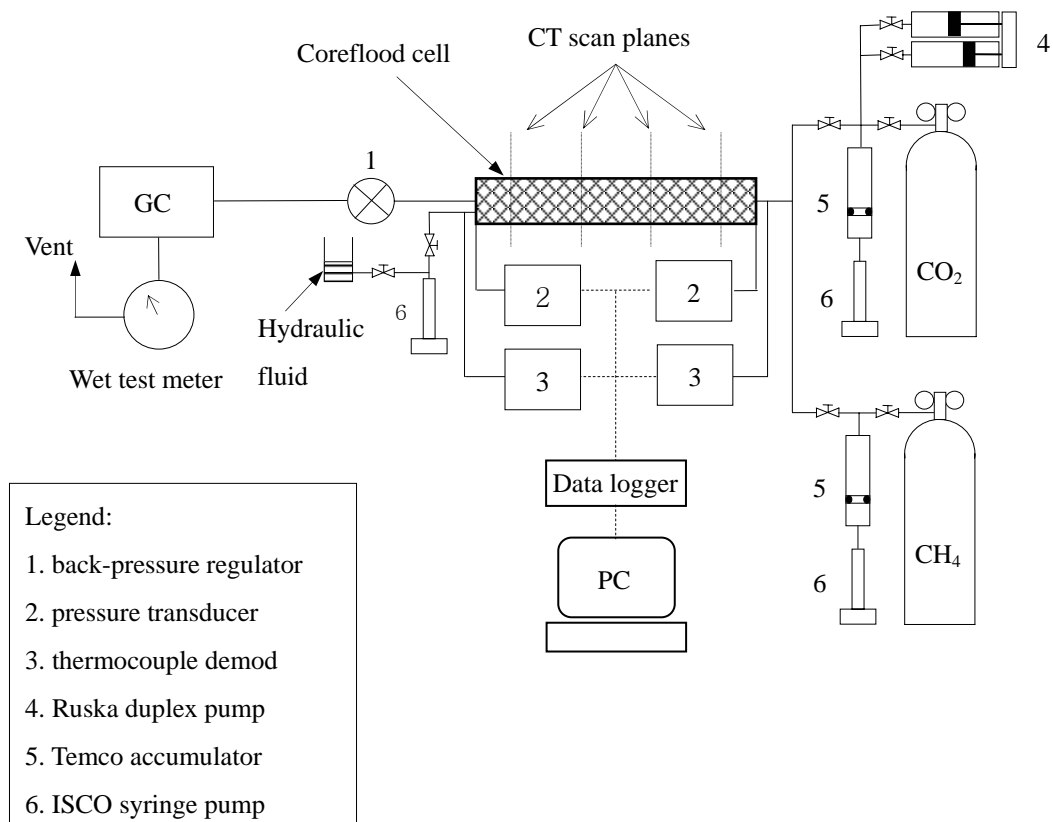
Fig. 3.1 – Schematic diagram of supercritical carbon dioxide coreflood apparatus.

TABLE 3.1— LIST OF EQUIPMENT USED

HPLC pump	ISCO syringe pump, model 314, range up to 3.33 cc/min.
Accumulator	Temco, model CF50-200-6, max. pressure 5,000 psi at 350°F .
Ruska pump	Ruska proportioning pump, model 2237-91627, max. pressure 12,000 psi, range up to 10 cc/min.
Back pressure regulator	Tescom Corp., model 26-1722-24, max. pressure 6,000 psi.
Pressure transducer	Omega, model PX 621, max. pressure 10,000 psi.
Thermocouple	Omega, J-type.
Coreflood cell	Custom made, aluminum 7075-T6, 53.5 cm (21 in.) long by 9.53 cm (3.75 in.) OD with wall thickness of 0.75 cm (1.91 in.).
Air blower	Master appliance, model VT-750C, max temperature 1,000°F.
X-ray CT scanner	Universal Systems, model HD-350E.
Wet test meter	American Meter Company, model P-2991.
Data logger	Hewlett-Packard data acquisition/switch unit, model 34970A.
Gas chromatograph	Carle analytical gas chromatograph, model series SX.
Integrator	Spectra-Physics, model SP4100 computing integrator.
Hydraulic oil	*Mobil DTE 26* hydraulic oil.

Fig. 3.2 – Temco accumulator connected to an ISCO syringe water pump.

After introducing the gas into the accumulator, the gas pressure is slowly increased to the desired level by injecting water below the piston in the accumulator.

3.1.2 Coreflood Cell

The coreflood cell, measuring 21 in. (53.3 cm) long with an OD of 3.3 in. (8.38 cm) and wall thickness of 0.75 in. (1.91 cm), is constructed of aluminum (transparent to x-ray CT scanning), and is machined out of a solid cylindrical block of aluminum 7075-T6 to withstand the high temperature and pressure (**Fig. 3.3**).

A carbonate core measuring 1 ft (30.5 cm) long and 1 in. (2.54 cm) in diameter is inserted into a viton Hassler sleeve with both ends secured to plungers in the cell. The cell is placed inside an aluminum trough that is fixed in a horizontal position to the moveable CT scanner sample table. The trough is adjusted so that the cell lies in the center of the scanner gantry aperture. The cell and trough are wrapped with 4 inch-thick *Fiberfrax* insulation (**Fig. 3.4**). Hot air from a temperature-regulated blower (*Master* Varitemp Heat Gun VT-750C) is blown from both sides of the trough. In this manner, the desired cell temperature can be obtained. The system is pressurized with nitrogen to test for leaks and then displaced to methane.

Fig. 3.3 – Coreflood cell (aluminum 7075-T6).

Fig. 3.4 – Coreflood cell with 4 inch- thick Fiberfrax insulation.

3.1.3 X-ray CT Scanner

The x-ray CT scanner is a Universal Systems HD200 with 760 diode detectors, giving a cross-sectional resolution of about 0.3 mm by 0.3 mm (**Fig. 3.5**). A new x-ray CT scanner (HD-350E) was installed in June 2002 (**Fig. 3.6**). Most remarkable change of new x-ray CT scanner is the image storage capacity. The HD-350E has about 300 times bigger storage capacity than the HD 200. In addition, the HD-350E can scan as fast as 1 sec/scan, has 75 cm diameter gantry, and more automation.

Fig. 3.5 – X-ray CT scanner (HD200).

Fig. 3.6 – X-ray CT scanner (HD-350E).

3.1.4 Production and Data Recording Systems

Produced gas volume, component, and composition are measured using a wet test meter and a Carle SX gas chromatograph with a Spectra Physics SP4100 integrator, respectively (**Fig. 3.7**). From these data, we can calculate the methane recovery factor at CO_2 breakthrough. The cell outlet pressure is set to the desired level with the aid of a *Temco* backpressure regulator. Pressure and temperature readings from two pressure

transducers (*Omega* PX 621) and two thermocouples (*Omega* J type) are recorded in 10-second intervals using a *HP* 34970A data logger in conjunction with a personal computer.

Fig. 3.7 – Carle SX gas chromatograph with a Spectra Physics SP4100 integrator.

3.2 Procedure

A typical experiment is conducted as follows. The core is first flushed with methane. With the backpressure regulator closed, the coreflood cell is slowly charged up with methane from the accumulator until the desired pressure is reached. While injecting methane into the cell, high-temperature *Mobil DTE 26* hydraulic oil is injected into the Hassler sleeve-inner cell wall annulus to maintain an overburden pressure differential of 300 psi. To increase cell temperature to the required value, hot air from two temperature-regulated blowers is applied to the coreflood cell inside of the trough. When pressure and temperature reach the desired experimental conditions, carbon dioxide is then injected into the cell at a constant rate of 0.25 ml/min. The composition of the produced gas is measured by a gas chromatograph and recorded on the integrator. The amount of produced gas is measured by a wet test meter. From these data, the recovery of methane at CO_2 breakthrough time is calculated. Cross-sectional CT scans of the cell are made three times during an experimental run: at start of the run, at carbon dioxide breakthrough, and at the end of the run. The CT scan images provide core porosity and fluid saturation data and help corroborate the dispersion and displacement of methane as inferred from gas compositional data and analysis. CT scan longitudinal section values of porosity and fluid saturation are calculated as follows.

$$\phi_{x,y} = \frac{CT_{x,y}^{100\%\,water} - CT_{x,y}^{dry}}{CT_{water} + 1000}$$
………………………………. (3.1)

where:

$CT_{x,y}^{100\%\,Water}$ is CT number of core saturated with 100 % water at x, y position.

$CT_{x,y}^{dry}$ is CT number of dry core at x, y position.

CT_{water} is CT number of water used to calculate $CT_{x,y}^{100\%\,Water}$.

$$S_{x,y}^{CO_2} = \frac{CT_{x,y}^{CO_2} - CT_{x,y}^{dry}}{\phi_{x,y}\left(CT_{CO_2} + 1000\right)} \qquad \ldots\ldots\ldots\ldots\ldots\ldots\ldots\ldots\ldots\ldots\ldots\ldots \qquad (3.2)$$

where:

$CT_{x,y}^{CO_2}$ is CT number of core saturated with CO_2 at x, y position.

$CT_{x,y}^{dry}$ is CT number of dry core at x, y position.

CT_{CO_2} is CT number of CO_2 used to calculate $CT_{x,y}^{CO_2}$.

$\phi_{x,y}$ is porosity at x, y position.

A run is terminated when the produced gas is practically 100% carbon dioxide for all practical purpose.

CHAPTER IV

EXPERIMENTAL RESULTS

A total of 22 runs have been made (**Table 4.1**): nine runs at 20°C (68°F), four runs at 40°C (104°F), four runs at 60°C (140°F), and five runs at 80°C (176°F). For each temperature, the cell pressure is varied, ranging from 500 psig (3.55 MPa) to 3000 psig (20.79 Mpa). Dispersion coefficients of each runs are relatively small, ranging from 0.01 to 0.3 cm^2/min. As a result of the stable displacement by carbon dioxide, the methane recovery at carbon dioxide breakthrough is high, ranging from 72.9 % to 87.2 % of OGIP except for run 33 (61.8 %).

The core in run 33 contained connate water to check the effects on dispersion coefficient and recovery factor caused by CO_2 dissolution in a wet carbonate. The core was first evacuated using a vacuum pump, and then saturated with water. Methane is then injected into the core until no water is produced, thus obtaining connate water saturation in the core. The run is then made with injection of supercritical CO_2. By comparing the results of run 31 and run 33, these effects can be explained because experimental conditions (temperature and pressure) between run 31 and run 33 are the same except the core in run 33 has connate water.

Dispersion coefficient obtained in run 33 is 0.15 cm^2/min, similar to that of run 31 (0.17 cm^2/min), but recovery factor at CO_2 breakthrough in run 33 is much lower than that of run 31 because of the smaller hydrocarbon pore volume.

The fundamental problem with injection of carbon dioxide into reservoirs containing carbonates is that it will react with the formation water resulting in the dissolution of carbonates until an equilibrium is reached between the fluid and rock (Eq. 4.1).

$$CO_2 + H_2O + CaCO_3 \rightarrow Ca^{2+} + 2HCO_3^- \qquad \dots\dots\dots\dots \qquad (4.1)$$

Our co-worker (Dr. John Morse in the Department of Oceanography at Texas A&M University) found limited dissolution of carbonate occurred in cases where a small amount of connate water was present and found no more dissolution after equilibrium is reached between the fluid and rock.

TABLE 4.1 – SUMMARY OF EXPERIMENTAL RUNS

Run no.	Temp., °C	Press., psig	Properties of C_1				C_1 prod. at CO_2 b/t		CO_2 b/t, min	Dispers. coeff., cm^2/min
			P_{pr}	T_{pr}	z	OGIP,SL	SL	% OGIP		
9	20	1,027	1.56	1.54	0.865	3.683	3.135	85.1	125	0.100
10	20	2,000	3.02	1.54	0.795	7.749	5.660	73.0	160	0.025
14	20	1,000	1.52	1.54	0.870	3.579	2.755	77.0	120	0.100
15	20	1,001	1.52	1.54	0.870	3.582	2.620	73.1	120	0.100
16	20	2,000	3.02	1.54	0.800	7.727	5.950	77.0	150	0.028
17	20	2,000	3.02	1.54	0.800	7.727	5.635	72.9	155	0.032
18	20	3,000	4.51	1.54	0.810	11.42	9.125	79.9	170	0.010
19	20	3,000	4.51	1.54	0.810	11.42	9.185	80.4	170	0.011
28	20	500	0.77	1.54	0.930	1.698	1.400	82.4	105	0.150
20	40	2,700	4.06	1.64	0.840	9.283	7.840	84.5	155	0.021
22	40	2,200	3.32	1.64	0.840	7.573	6.280	82.9	130	0.030
24	40	1,700	2.57	1.64	0.860	5.727	4.935	86.2	100	0.070
26	40	1,200	1.82	1.64	0.880	3.965	3.350	84.5	65	0.120
21	60	2,700	4.06	1.75	0.880	8.330	7.145	85.8	135	0.040
23	60	2,200	3.32	1.75	0.880	6.795	5.925	87.2	120	0.060
25	60	1,700	2.57	1.75	0.890	5.202	4.515	86.8	90	0.120
27	60	1,200	1.82	1.75	0.910	3.604	3.130	86.8	55	0.200
29	80	2,700	4.06	1.85	0.925	7.623	6.250	82.0	105	0.070
30	80	2,200	3.32	1.85	0.921	6.250	5.170	82.7	75	0.110
31	80	1,700	2.57	1.85	0.924	4.819	4.045	83.9	60	0.170
32	80	1,200	1.82	1.85	0.937	3.368	2.850	84.6	30	0.300
33	80	1,700	2.57	1.85	0.924	3.739	2.310	61.8	55	0.150

4.1 Dispersion Coefficient

   Fig. 4.1 graphs the mole percent of carbon dioxide as a function of time for the nine runs at 20°C - where carbon dioxide is either liquid (runs 9-19) or gas (run 28) depending on the pressure.

   Best-fit lines represent the analytical solution for the best value of the coefficient of dispersion of carbon dioxide.   Because the values are relatively small, ranging from 0.01 to 0.04 cm^2/min, all graphs look very steep and the methane appears to be stably displaced by the injected supercritical CO_2.   In particular, dispersion coefficient of run 28 is larger than the others because liquid CO_2 is much denser than gaseous CO_2.

   Fig. 4.2 shows similar graphs for the eight runs at 40°C where the carbon dioxide is at supercritical conditions.   From the graphs of carbon dioxide concentration versus time data, breakthrough time of carbon dioxide may be inferred by visual inspection.

   Fig. 4.3 shows similar graphs for the eight runs at 60°C where the carbon dioxide is at supercritical conditions.

   Fig. 4.4 shows similar graphs for the five runs at 80°C where the carbon dioxide is at supercritical conditions.   Note that the core in run 33 has connate water.
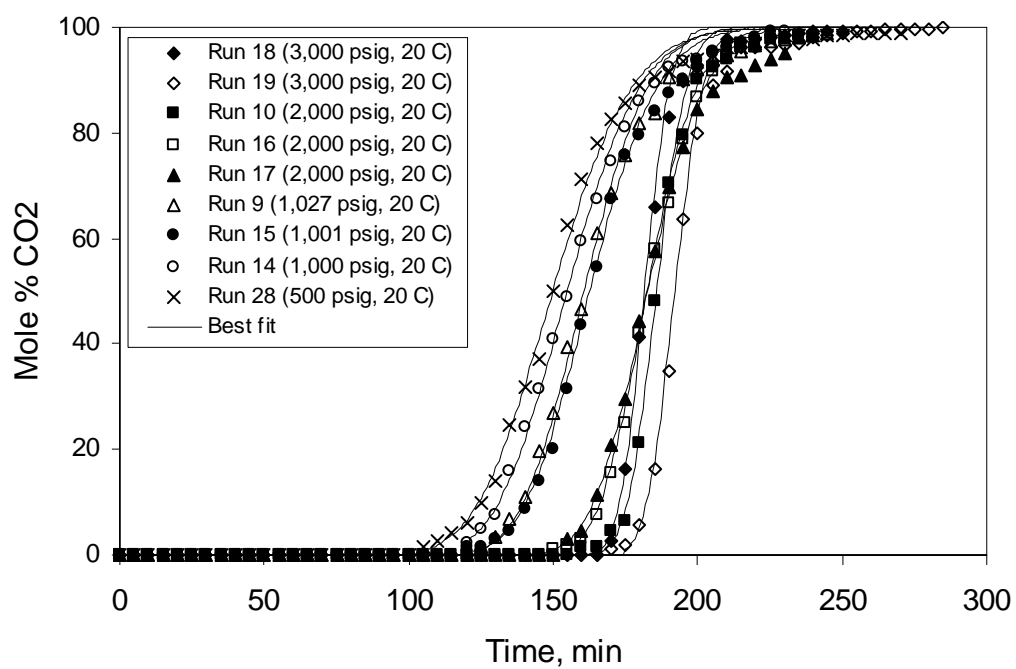
Fig. 4.1 – Produced CO$_2$ concentration versus time for runs at 20°C.
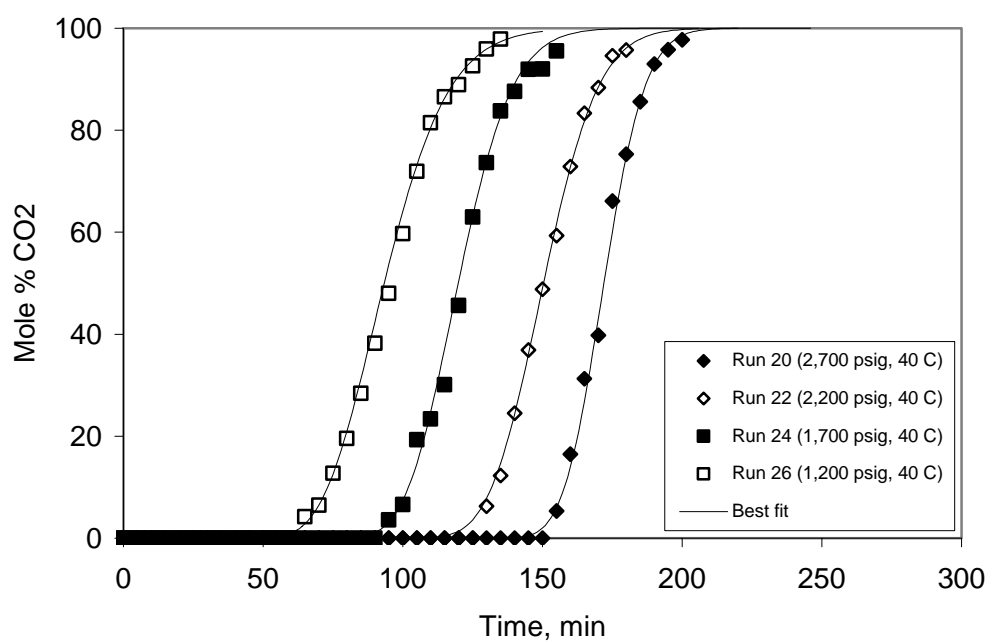
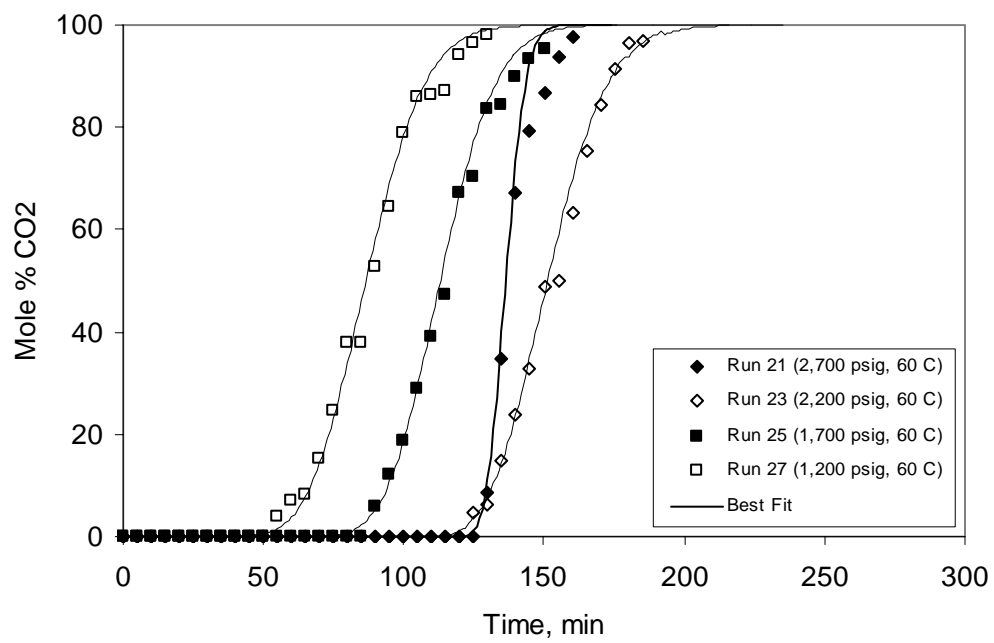**Fig. 4.2 – Produced CO$_2$ concentration versus time for runs at 40°C.**

Fig. 4.3 – Produced CO$_2$ concentration versus time for runs at 60°C.
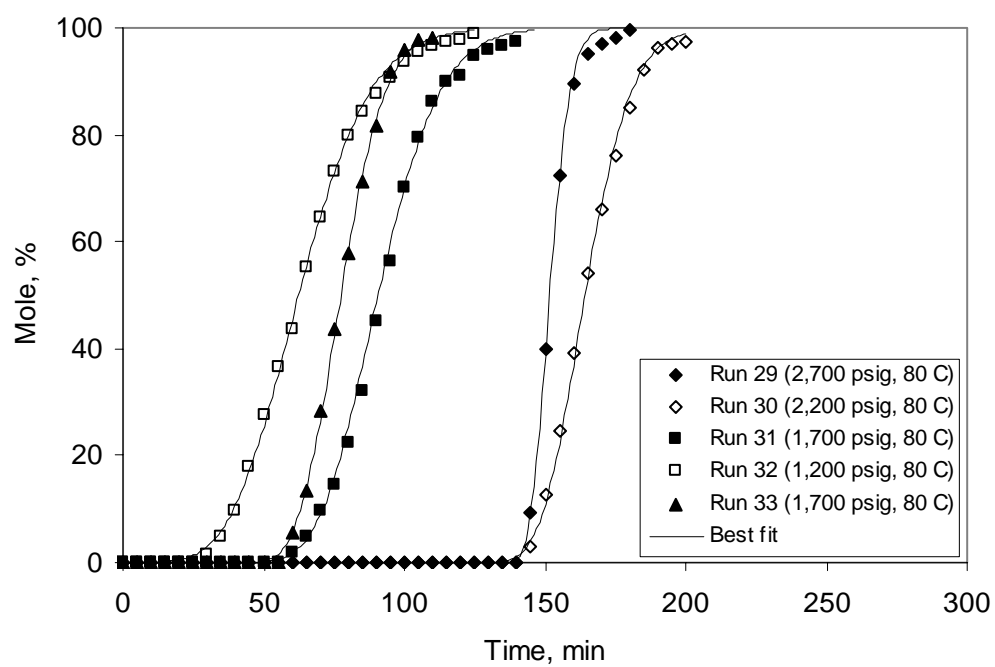
Fig. 4.4 – Produced CO$_2$ concentration versus time for runs at 80°C.

4.2 Breakthrough Times

Figs. 4.1, 4.2, 4.3, and 4.4 indicate that the breakthrough times of CO_2 vary from 55 min to 170 min. However, we set the supercritical CO_2 injection rate to 0.25 ml/min using the water syringe pump (displacing the CO_2 in the accumulator) for all runs. Thus CO_2 breakthrough time in all runs should be same. This probably means that the CO_2 injection rate varies in each run due to cell pressure variation resulting from continuous adjustment of the backpressure regulator during a run. **Fig. 4.5** shows pressure data for Run 9 (1,027 psig and 20°C). Initially, we set core pressure to 1,027 psig. But, the core pressure varies somewhat during the experiment because the backpressure regulator is fully hand-operated. This pressure fluctuation causes the injection rate fluctuations and thus different CO_2 breakthrough times.

Since we have measured the volume of methane produced, it is possible to calculate the CO_2 injection rate based on methane volume produced at CO_2 breakthrough.
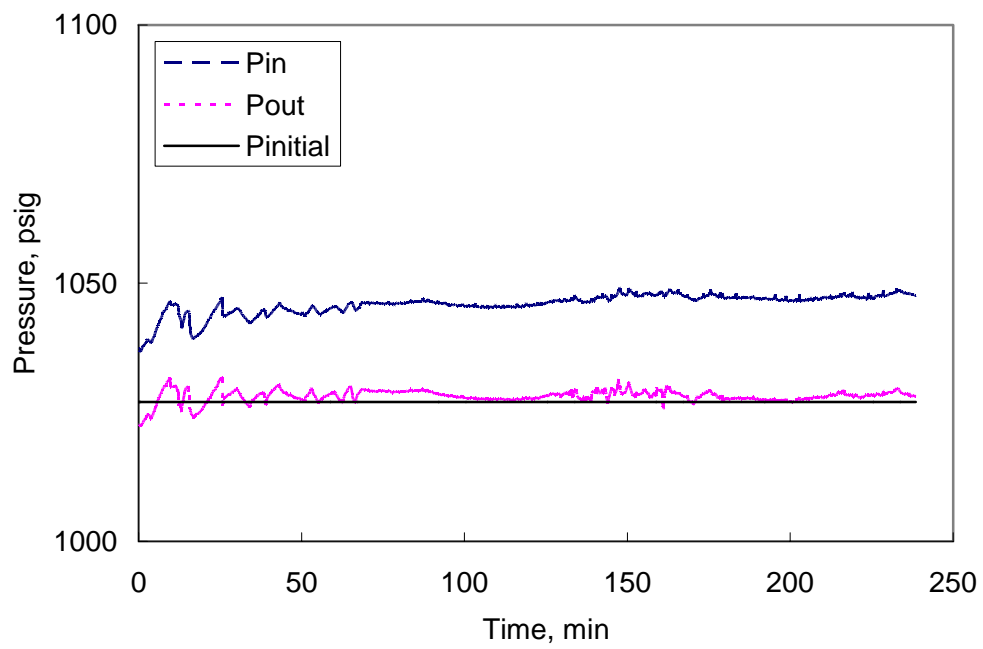
Fig. 4.5 – Pressure data for Run 9 (1,027 psig and 20°C).

The actual CO_2 injection rate has thus been estimated as follows, using run 9 as an example.

Remaining C_1 vol. (at cell conditions) at CO_2 b/t

$\qquad$ = vol. at std. conditions $\times$ z $\times$ (T/520) $\times$ (14.7/P)

$\qquad$ = 548 ml $\times$ 0.865 $\times$ (528°R /520°R) $\times$ (14.7 psia/1041.7 psia) = 6.8 ml

Pore vol. $\quad$ = 10.3 ml (dead vol.) + π (2.54/2)^2 cm^2 $\times$ 30.48 cm $\times$ 0.23 (porosity from CT

$\qquad$ scan)

$\qquad$ = 45.8 ml

C_1 saturation in cell at CO_2 b/t, S_g = 6.8 ml/45.8 ml = 15%

CO_2 P.V. at b/t = P.V. $\times$ (1 – S_g) = 45.8 ml $\times$ (1- 0.15) = 38.9 ml

Ave. CO_2 injection rate = 38.9 ml/125 min = 0.31 ml/min

Thus, CO_2 b/t time = 38.9 ml/(0.31 ml/min)= 125 min

The calculated CO_2 breakthrough times for all runs are listed in **Table 4.2** and compared against observed values in Fig. **4.6**.

TABLE 4.2 – ESTIMATION OF METHANE SATURATION IN CORE AND BREAKTHROUGH TIME

Run no.	Remaining C_1 vol. at CO_2 b/t, ml		Sg(%)	CO_2 P.V. at b/t, ml	CO_2 inj. ml/min	CO_2 b/t time, min	
	Std. cond.	Cell cond.				Calc.	Actual
9	548	6.8	14.8	39.0	0.31	126	125
10	2,089	12.3	26.9	33.5	0.21	159	160
14	824	10.5	23.0	35.3	0.29	122	120
15	962	12.3	26.9	33.5	0.28	119	120
16	1,777	10.5	23.0	35.3	0.24	147	150
17	2,092	12.4	27.1	33.4	0.22	152	155
18	2,295	9.2	20.1	36.6	0.22	167	170
19	2,235	9.0	19.6	36.8	0.22	167	170
20	1,443	6.7	14.6	39.1	0.25	167	155
21	1,185	5.7	12.5	40.1	0.30	136	135
22	1,293	7.3	16.0	38.5	0.30	131	130
23	870	5.2	11.3	40.6	0.34	122	120
24	792	5.9	12.9	39.9	0.40	100	100
25	687	5.3	11.6	40.5	0.45	91	90
26	615	6.7	14.5	39.1	0.60	64	65
27	474	5.3	11.6	40.5	0.74	55	55
28	298	8.0	17.5	37.8	0.36	104	105
29	1,373	7.0	15.3	38.8	0.37	104	105
30	1,080	6.7	14.6	39.1	0.52	77	75
31	774	6.2	13.6	39.6	0.66	59	60
32	518	6.0	13.0	39.8	1.33	31	30
33	1,429	11.5	25.1	34.3	0.57	61	60

The good agreement between the two sets of values confirms the accuracy of the core porosity value (0.23) measured with the aid of the CT scanner.

Figs. **4.7**, **4.8**, **4.9**, and **4.10** show corrected Figs. **4.1**, **4.2**, **4.3**, and **4.4** at the same injection rate (0.25 ml/min) through above calculation.
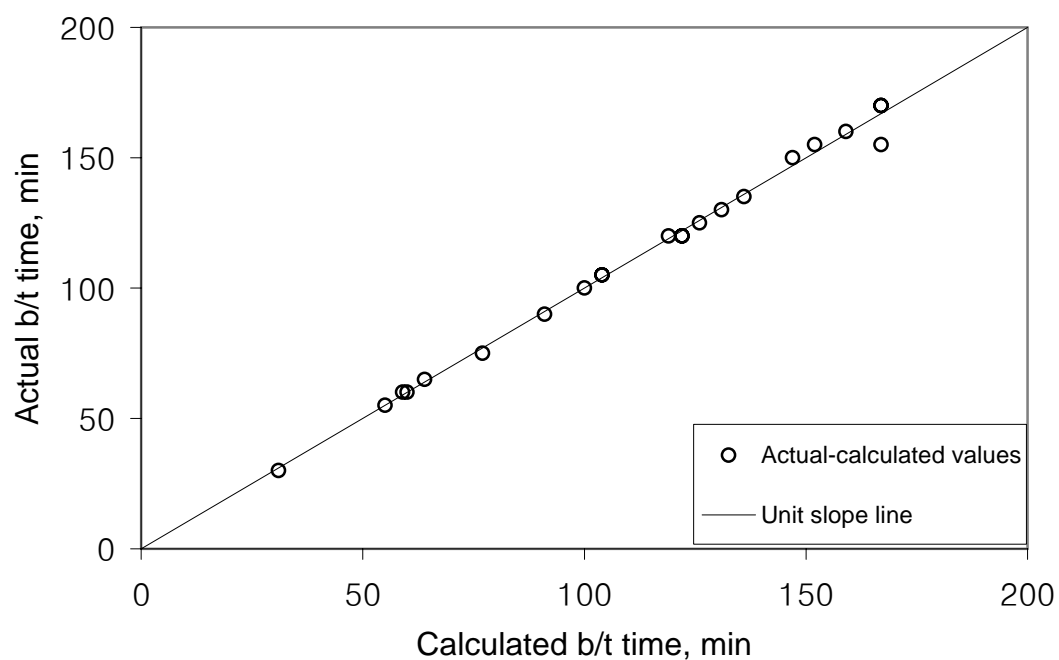

Fig. 4.6 – Comparison of observed and calculated CO_2 breakthrough times.
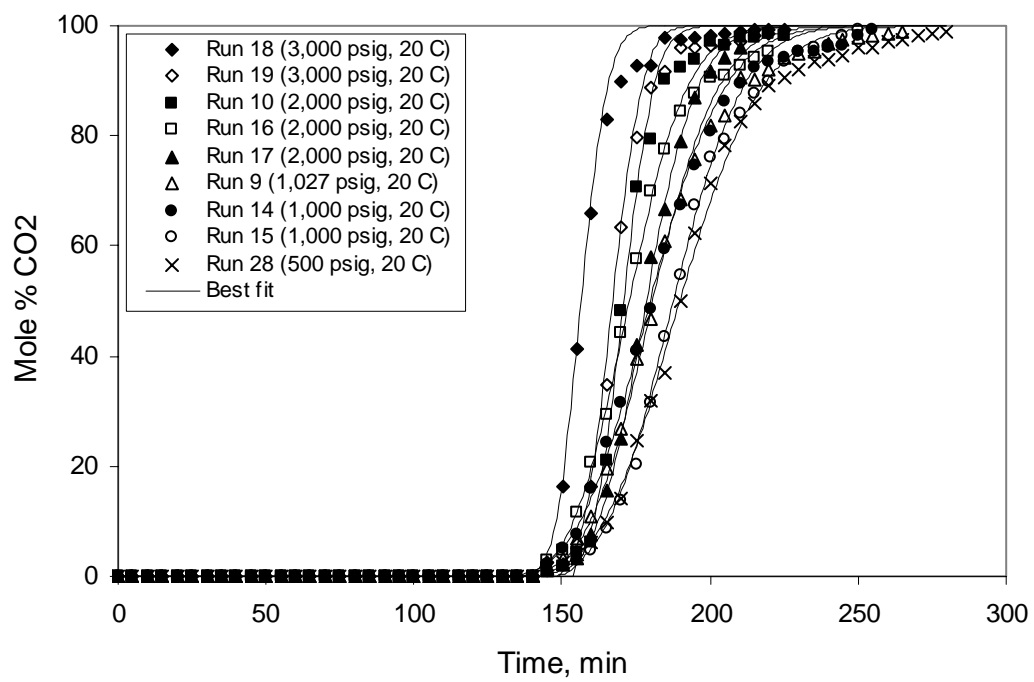
Fig. 4.7 – CO$_2$ concentration versus time for runs at 20°C.
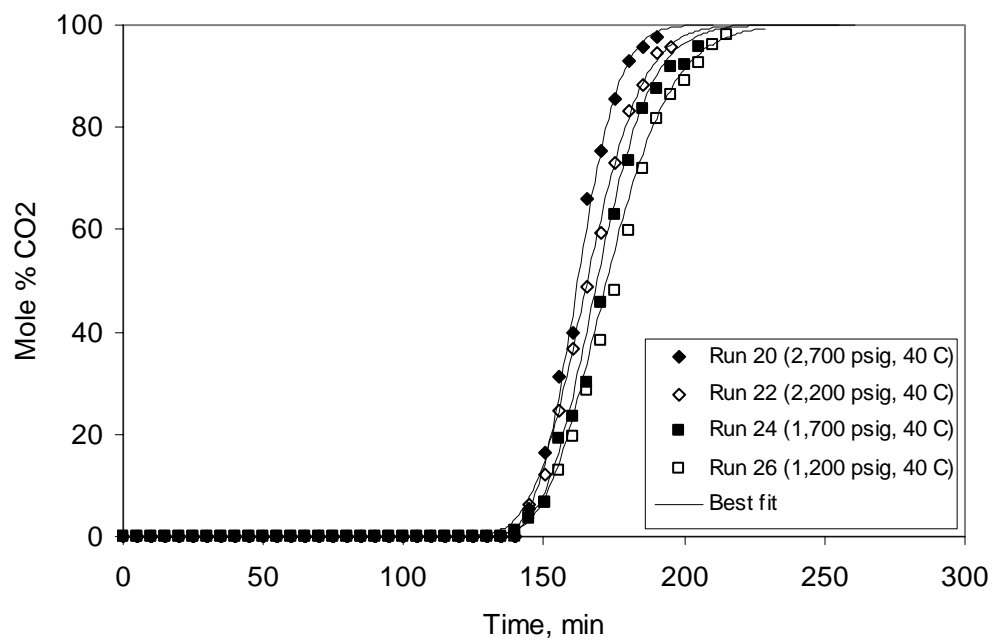
Fig. 4.8 – CO$_2$ concentration versus time for runs at 40°C.
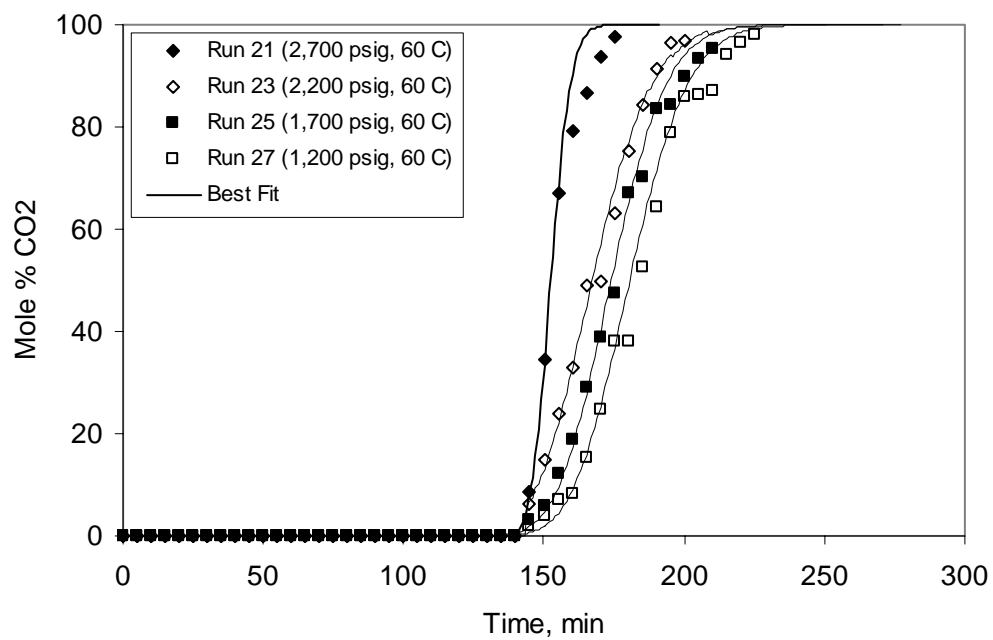
Fig. 4.9 – CO$_2$ concentration versus time for runs at 60°C.
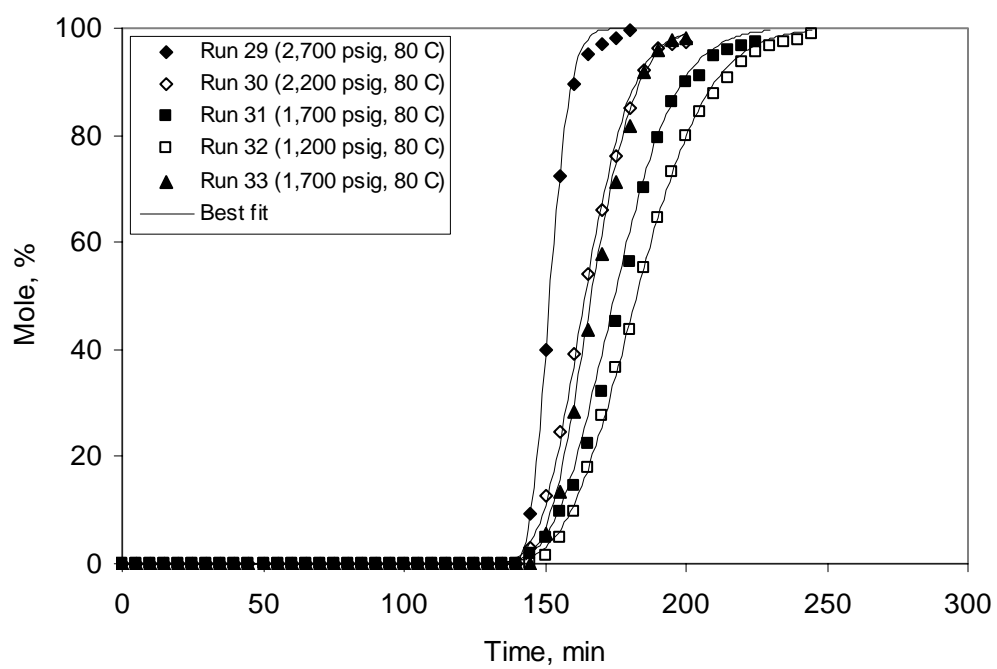
Fig. 4.10 – CO$_2$ concentration versus time for runs at 80°C.

Fig. 4.11 and Fig. 4.12 show dispersion coefficient with various pressures and temperatures. Dispersion coefficient is increased as temperature is increased at the same pressure and as pressure is decreased at the same temperature because the supercritical CO_2 has more gaseous form.
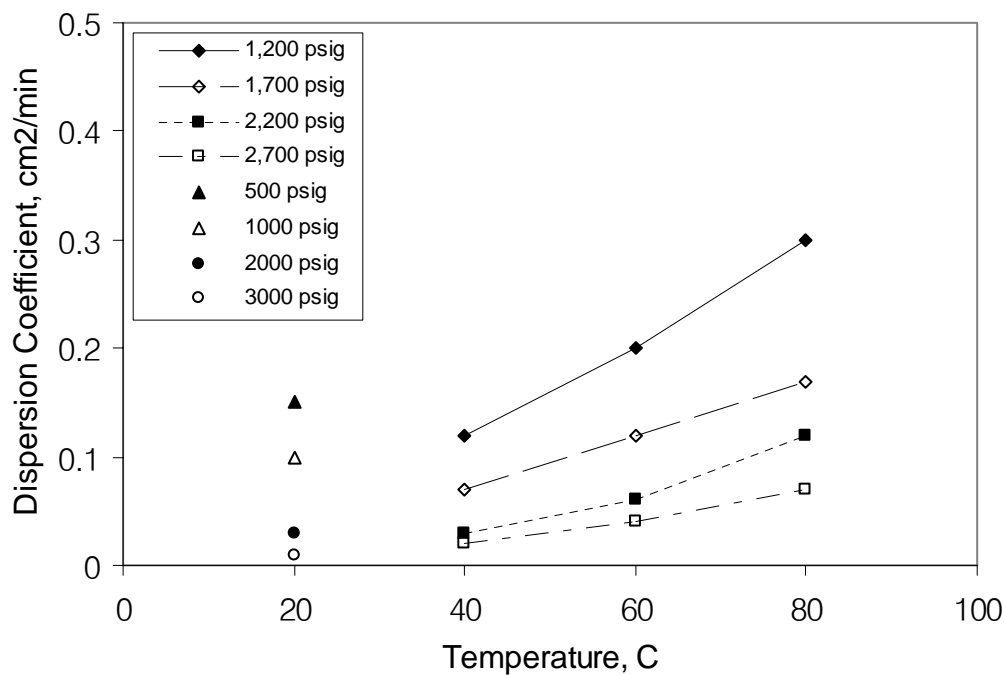
Fig. 4.11 – Dispersion coefficient versus temperature with various pressures.
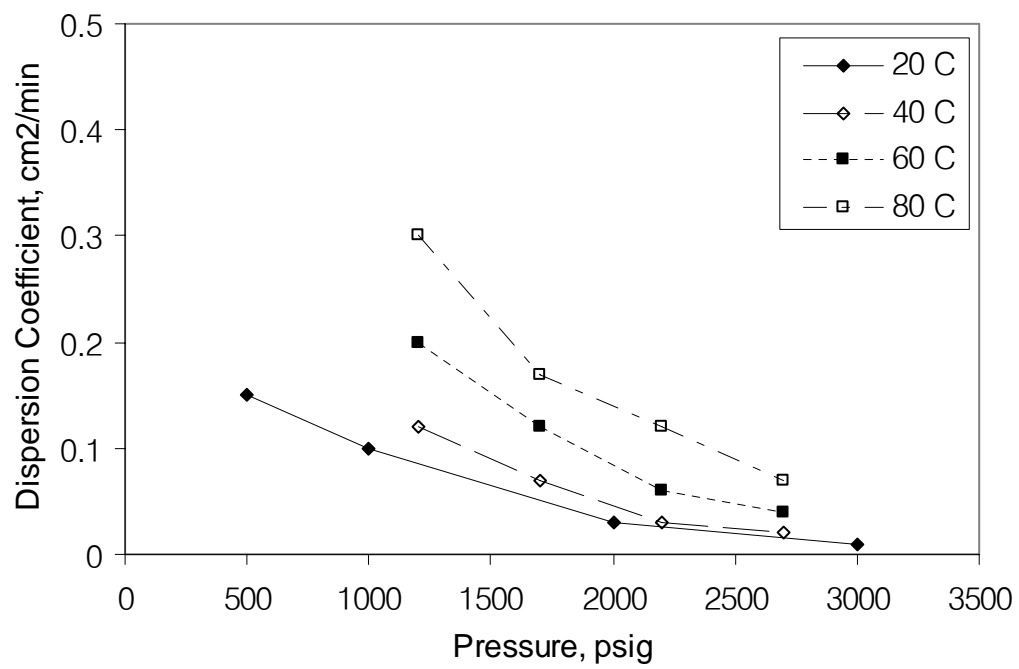
Fig. 4.12 – Dispersion coefficient versus pressure with various temperatures.

4.3 Rock Property and Fluid Saturation

The CT scan images provide core porosity and fluid saturation data and help corroborate the dispersion and displacement of methane as inferred from gas compositional data and analysis.

Fig. 4.13 shows CT scan images of a core at the beginning of experiment in case of Run 29 (2,700 psig, 80°C).   First image is scanned at outlet end and last image is at injection end.   Because a core is fully saturated with only methane at the beginning of experiment, we can say the series of blue color (low CT no.) means the part of high porous medium saturated with more methane and the series of green color (high CT no.) means low porous medium saturated with smaller amount of methane than the series of blue color.   Especially, red color (very high CT no.) means high density material (rock material) inside of core.

Fig. 4.14 shows CT scan images of core at CO_2 breakthrough in case of Run 29 (2,700 psig, 80°C).   A core must be scanned at the exactly same position three times: at start of the run, at carbon dioxide breakthrough, and at the end of the run to calculate core porosity and fluid saturation.   Compared with Fig. **4.13**, CT scan images of **Fig. 4.12** have more the series of green and red colors because large amount of methane with lower density is substituted with supercritical CO_2 with higher density injected from inlet end.

Outlet end

Injection end
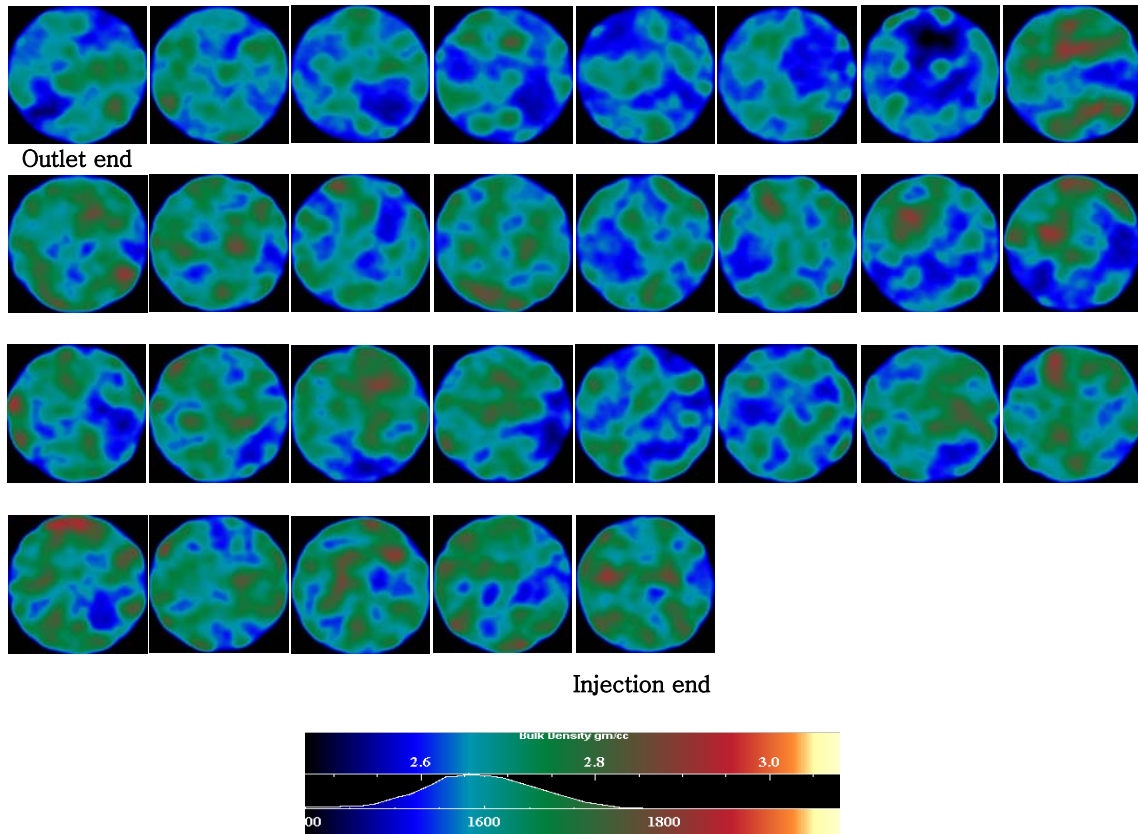
Fig. 4.13 – CT scan images of core at the beginning of experiment in case of Run 29 (2,700 psig, 80°C).

Outlet end

Injection end
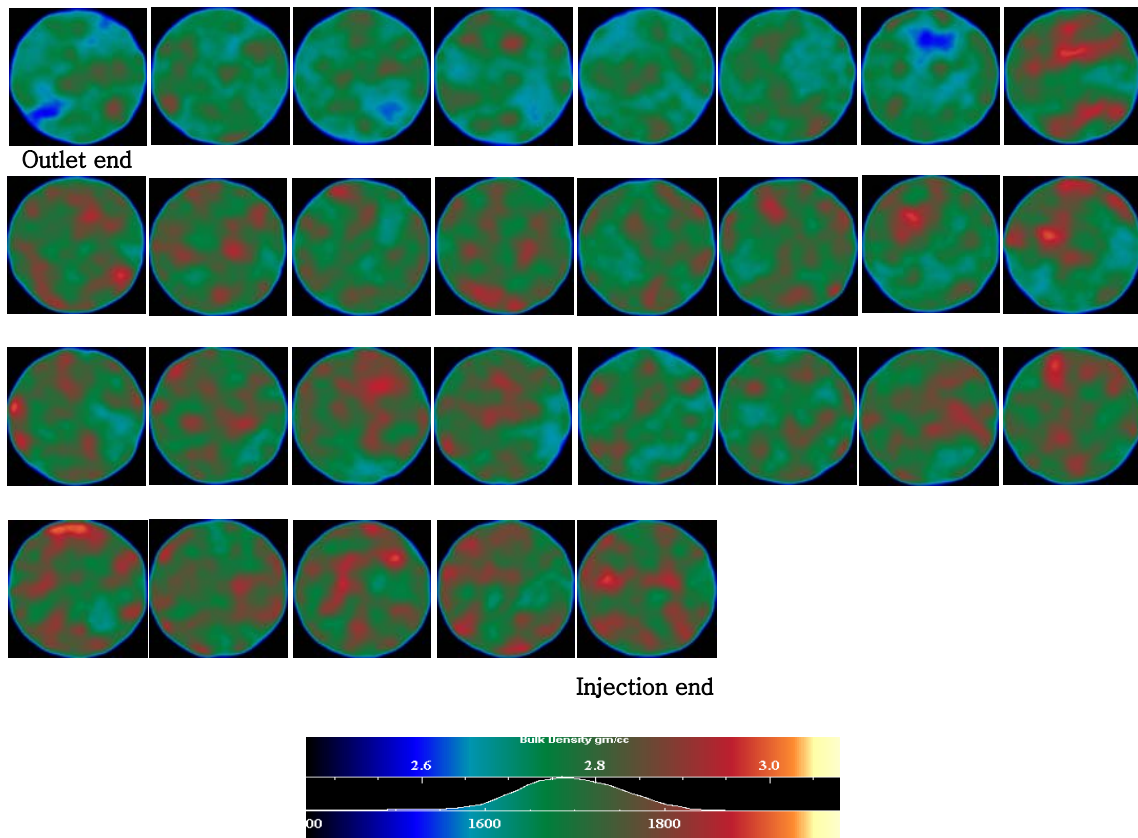
Fig. 4.14 – CT scan images of core at CO$_2$ breakthrough in case of Run 29 (2,700 psig, 80°C).

Outlet end
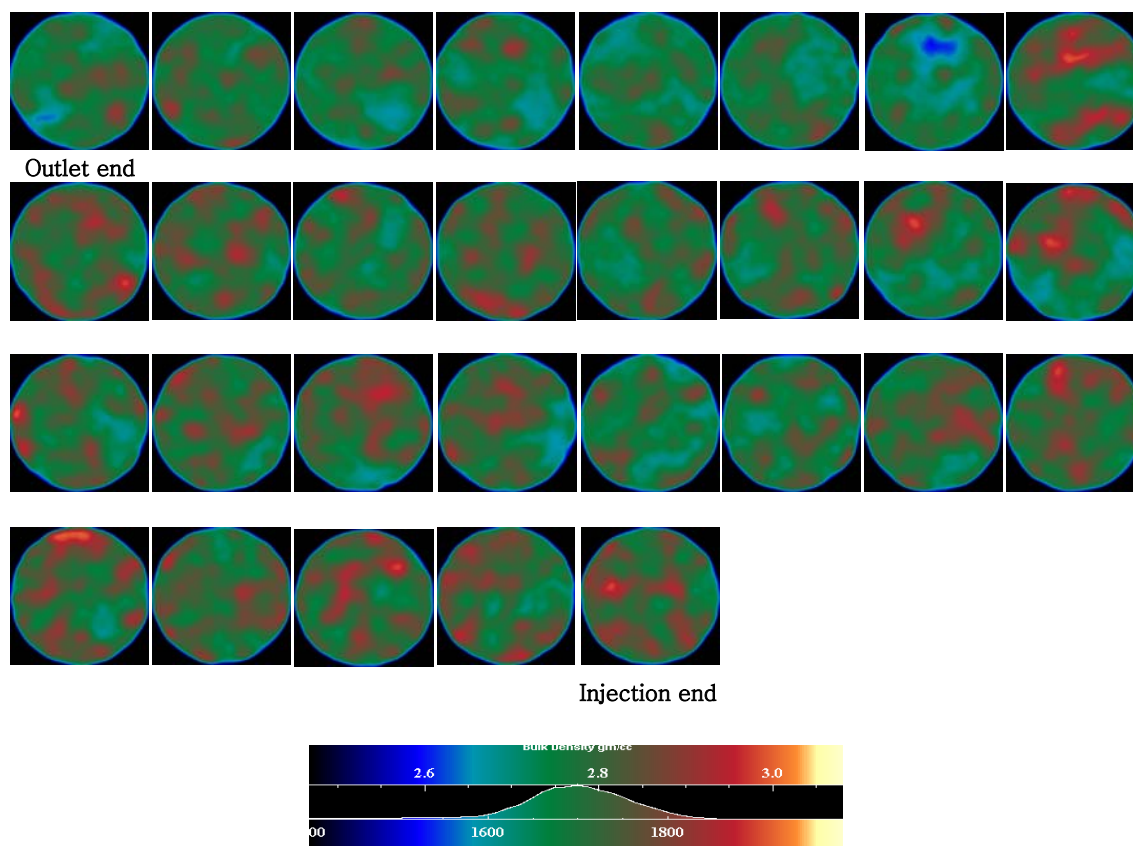
Injection end

Fig. 4.15 – CT scan images of core at the end of experiment in case of Run 29 (2,700 psig, 80°C).

Fig. 4.15 shows CT scan images of core at the end of experiment in case of Run 29 (2,700 psig, 80°C). CT scan images near injection end in **Fig. 4.15** are almost same as those of **Fig 4.14**, but CT scan images near outlet end in **Fig. 4.15** have more the series of green and red colors than those of **Fig. 4.14** because a core is fully saturated with supercritical CO_2 with higher density compared with the core at CO_2 breakthrough.

Fig. 4.16 shows CT scan images at first position in case of Run 29 (2,700 psig, 80°C) three times: (a) at the beginning, (b) at CO_2 breakthrough, and (c) at the end of experiment. From (a) to (c), the series of green and red color (high CT no.) are increased because large amount of methane with lower density is substituted with supercritical CO_2 with higher density.
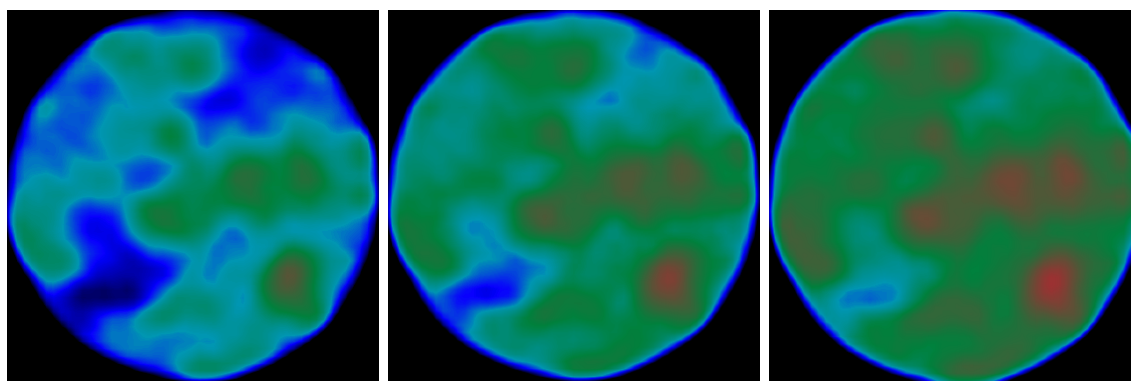
(a) at the beginning   (b) CO_2 breakthrough   (c) at the end of experiment

Fig. 4.16 – CT scan images at first position in case of Run 29 (2,700 psig, 80°C) three times: (a) at the beginning, (b) at CO_2 breakthrough, and (c) at the end of experiment.

Fig. 4.17 shows CT scan images at second position in case of Run 29 (2,700 psig, 80°C) three times: (a) at the beginning, (b) at CO_2 breakthrough, and (c) at the end of experiment. From (a) to (c), the series of green and red color (high CT no.) are increased because large amount of methane with lower density is substituted with supercritical CO_2 with higher density.

Compared with **Fig. 4.16**, the difference of color of CT images between (b) CO_2 breakthrough and (c) at the end of experiment in **Fig. 4.17** is very small. In other words, a core of second position at CO_2 breakthrough is almost fully saturated with supercritical CO_2 like the end of experiment.

Fig. 4.18 shows CT scan images at last position in case of Run 29 (2,700 psig, 80°C) three times: (a) at the beginning, (b) at CO_2 breakthrough, and (c) at the end of experiment. From (a) to (c), the series of green and red color (high CT no.) are increased because the amount of substituted supercritical CO_2 is increased with time. Compared with **Fig. 4.17**, CT images of (b) at CO_2 breakthrough and (c) at the end of experiment in **Fig. 4.18** are the same. In other words, a core at last position is fully saturated with supercritical CO_2.

(a) at the beginning   (b) CO_2 breakthrough   (c) at the end of experiment

Fig. 4.17 – CT scan images at second position in case of Run 29 (2,700 psig, 80°C): (a) at the beginning, (b) at CO_2 breakthrough, and (c) at the end of experiment.

(a) at the beginning   (b) CO_2 breakthrough   (c) at the end of experiment
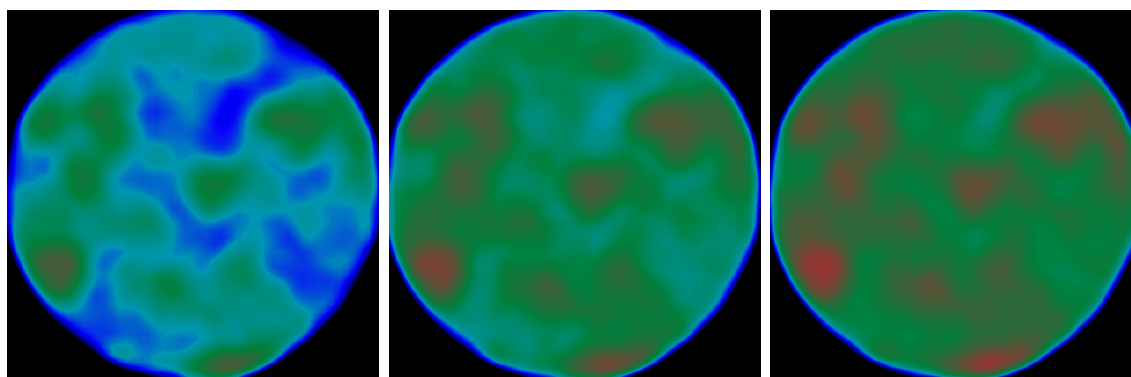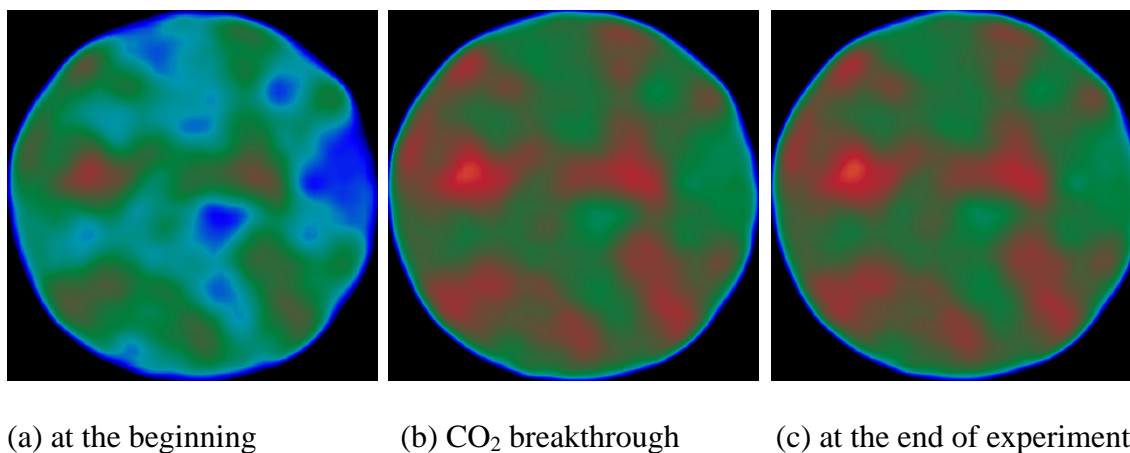
Fig. 4.18 – CT scan images at last position in case of Run 29 (2,700 psig, 80°C): (a) at the beginning, (b) at CO_2 breakthrough, and (c) at the end of experiment.

Fig. 4.19 shows color scales of CT images in case of Run 29 (2,700 psig, 80°C): (a) at the beginning, (b) at CO_2 breakthrough, and (c) at the end of experiment. Color scale at CO_2 breakthrough is shifted to right (high CT no.) compared with color scale at the beginning because of CO_2 saturation inside of core. But, color scale at the end of experiment is slightly shifted to right or almost same as that of CO_2 breakthrough. Only small difference in color scale between CO_2 breakthrough and the end of experiment is caused by CO_2 saturation inside of core at outlet end as shown in **Fig. 4.16**.

(a) Color scale of CT images at the beginning of experiment in case of Run29.

(b) Color scale of CT images at the CO_2 breakthrough in case of Run 29.
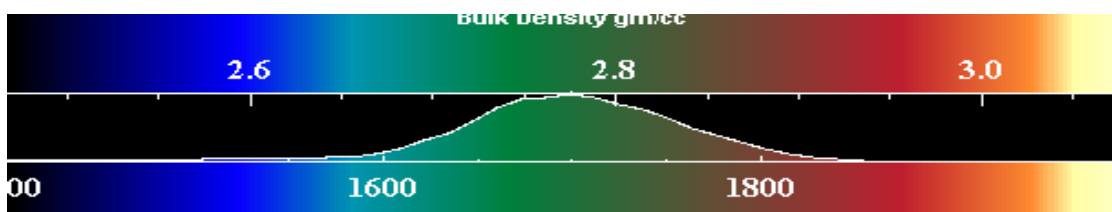
(c) Color scale of CT images at the end of experiment in case of Run 29.

Fig. 4.19 – Color scales of CT images in case of Run 29 (2,700 psig, 80°C): (a) at the beginning, (b) at CO_2 breakthrough, and (c) at the end of experiment.

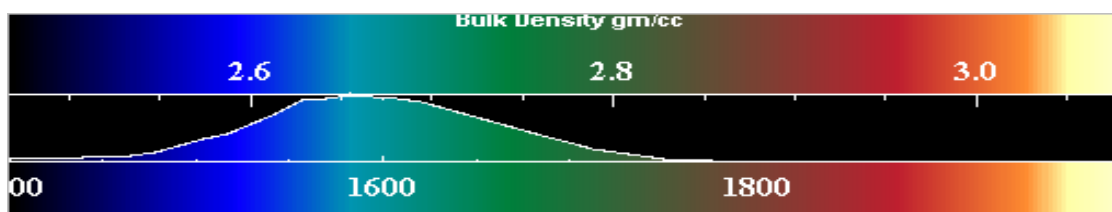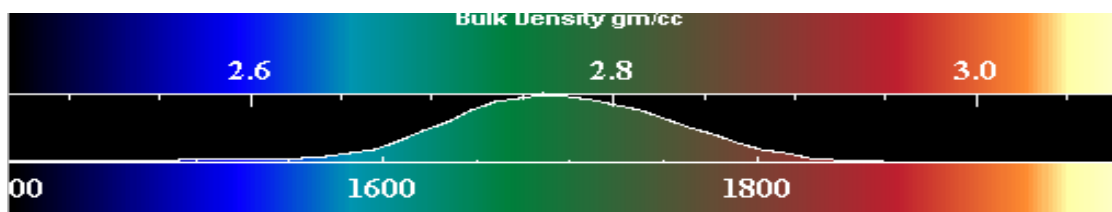CT scan longitudinal section value of porosity is calculated as follows.

$$\phi_{x,y} = \frac{CT_{x,y}^{100\% \, water} - CT_{x,y}^{dry}}{CT_{water} + 1000} \qquad \dots\dots\dots\dots\dots\dots\dots\dots\dots\dots\dots\dots \qquad (4.2)$$

where:

$CT_{x,y}^{100\% \, Water}$ is CT number of core saturated with 100 % water at x, y position.

$CT_{x,y}^{dry}$ is CT number of dry core at x, y position.

CT_{water} is CT number of water used to calculate $CT_{x,y}^{100\% \, Water}$.

Table 4.3 shows porosity of core calculated from x-ray CT scanner. For the accuracy of porosity calculation, we use two sets of CT number of core saturated with 100 % water at x, y position. As shown in **Table 4.3**, average porosity of core is identified as 0.23 in both cases.

TABLE 4.3 – POROSITY CALCULATION FROM X-RAY CT SCANNER

Dry			100% Water			100% Water					
Scan No.	Position (mm)	CT No.	Scan No.	Position (mm)	CT No.	Scan No.	Position (mm)	CT No.	Position (mm)	Porosity 1	Porosity 2
	280	1681.5	985		1927.6	996	280	1926.7	280	0.25	0.24
964	252	1663.2	986	252	1912.9	997	252	1913.5	252	0.25	0.25
965	224	1669.0	987	224	1918.1	998	224	1914.6	224	0.25	0.25
966	196	1623.2	988	196	1878.6	999	196	1884.6	196	0.26	0.26
967	168	1659.9	989	168	1913.8	1000	168	1907.3	168	0.25	0.25
968	140	1631.7	990	140	1890.2	1001	140	1889.2	140	0.26	0.26
969	112	1705.2	991	112	1900.9	1002	112	1907.4	112	0.20	0.20
970	84	1710.8	992	84	1909.4	1003	84	1907.2	84	0.20	0.20
971	56	1665.5	993	56	1871.4	1004	56	1884.6	56	0.21	0.22
972	28	1675.4	994	28	1885.8	1005	28	1874.9	28	0.21	0.20
973	0	1678.1	995	0	1855.8	1006	0	1847.2	0	0.18	0.17
									Average	0.23	0.23

Fig. 4.20 shows CT images of porosity profile calculated by porosity equation (Eq. 4.2) with the aid of *Voxelcalc* image processing software. In color scale, minimum value of porosity is about 0.1, maximum value is about 0.28, and average value of porosity is 0.23 same as that in **Table 4.3**.

The series of green (higher CT no.) means high porous medium and the series of blue color (lower CT no.) means low porous medium.

Fig. 4.21 shows porosity profile image compared with CT scan images at first position in case of Run 29 (2,700 psig, 80°C) three times: (a) at the beginning, (b) at CO_2 breakthrough, and (c) at the end of experiment.

We can see the series of green and red color (high CT no.) in CT images of (a) at the beginning, (b) at CO_2 breakthrough, and (c) at the end of experiment are shown as the series of blue color (low porosity) in porosity profile image and the series of blue color (low CT no.) are shown as the series of green color (high porosity) in porosity profile image.
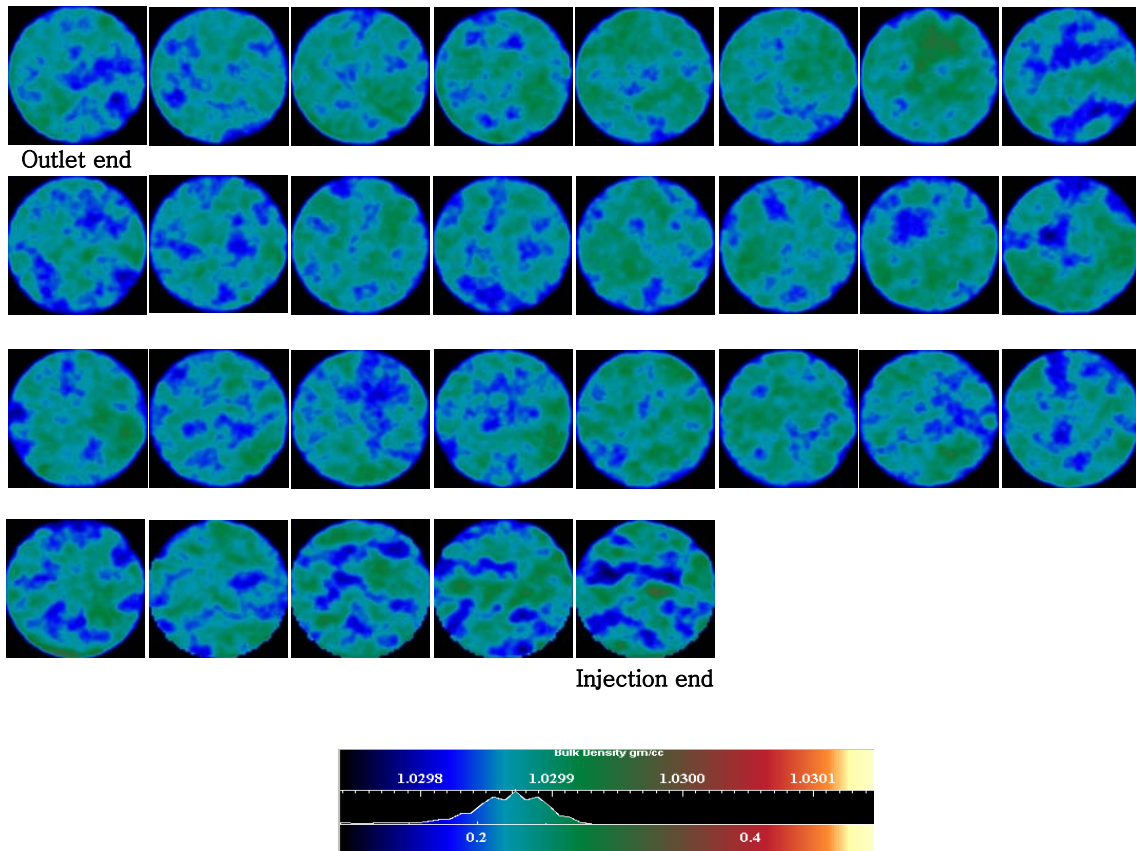
Fig. 4.20 – CT images of porosity profile using *Voxelcalc* software.

(a) at the beginning

(b) CO$_2$ breakthrough

(c) at the end of experiment
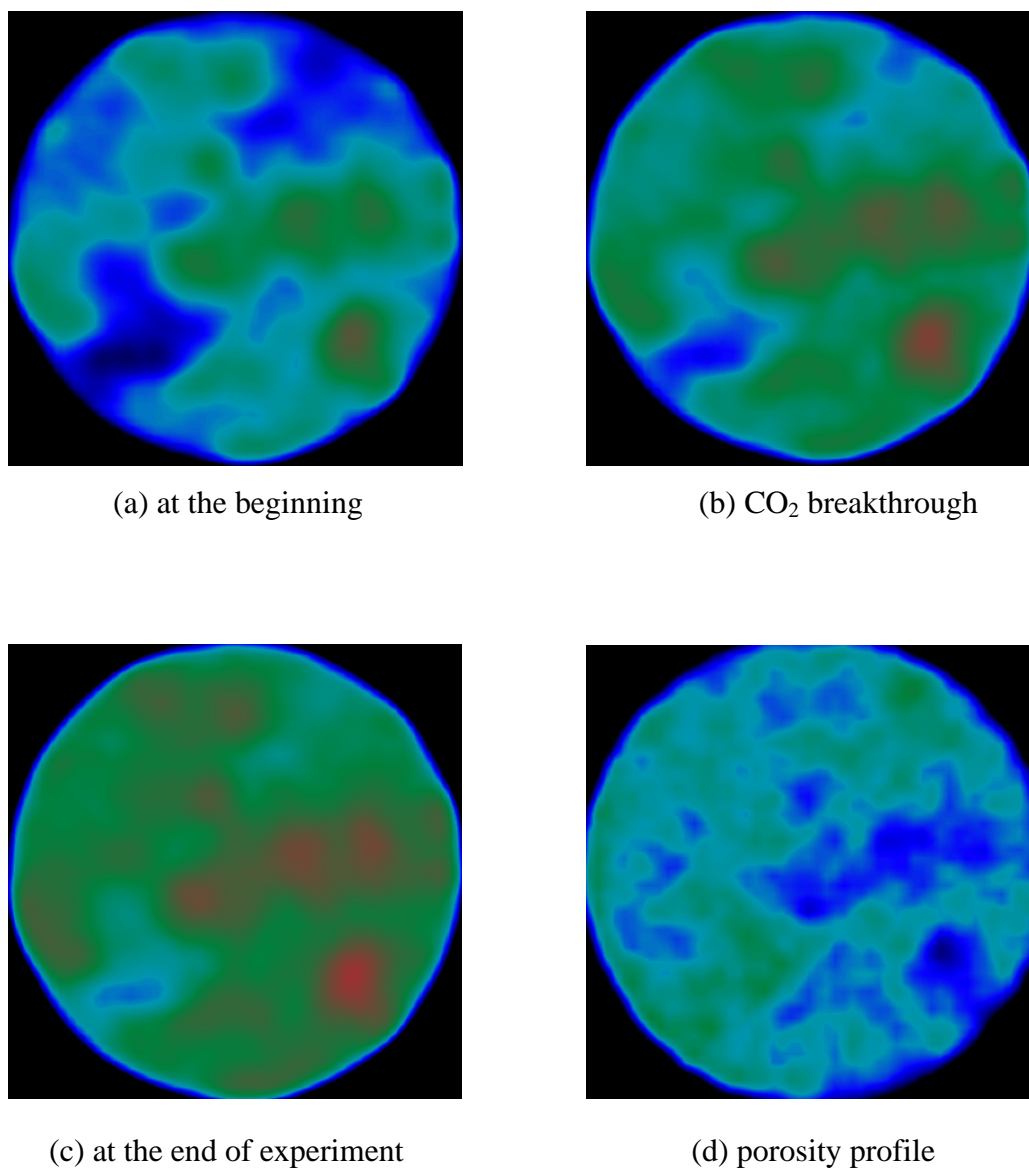
(d) porosity profile

Fig. 4.21 – Porosity profile compared with CT scan images at first position in case of Run 29 (2,700 psig, 80°C) three times: (a) at the beginning, (b) at CO$_2$ breakthrough, and (c) at the end of experiment.

Fig. 4.22 shows isosurface images of 3D porosity profiles using *Petro3D*: (a) porosity = 0.18, (b) porosity = 0.2, (c) porosity = 0.23, and (d) porosity = 0.25. These images could be very helpful to understand how porous medium is distributed inside the core.
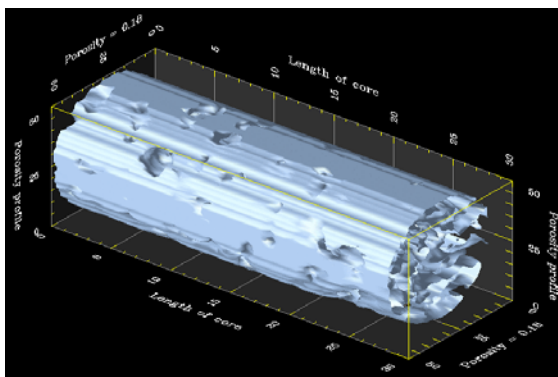
(a) Porosity = 0.18
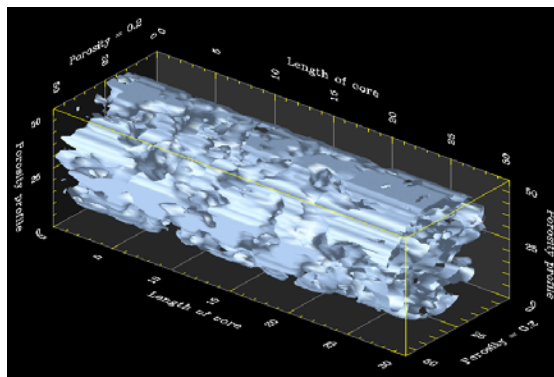
(b) Porosity = 0.2
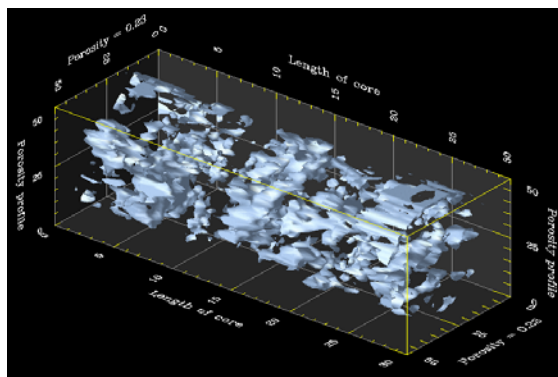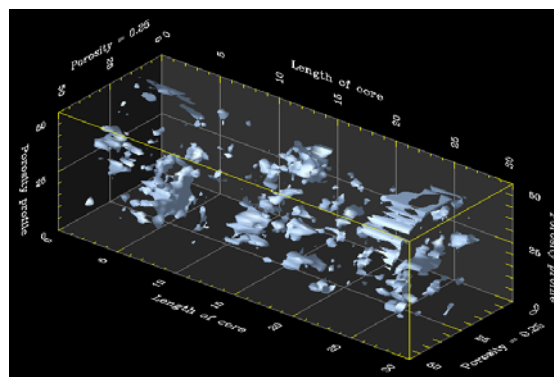
(c) Porosity = 0.23

(d) Porosity = 0.25

Fig. 4.22 – Isosurface images of 3D porosity profiles using *Petro3D* software: (a) porosity = 0.18, (b) porosity = 0.2, (c) porosity = 0.23, and (d) porosity = 0.25.

CT scan longitudinal section value of saturation is calculated as follows.

$$S_{x,y}^{CO_2} = \frac{CT_{x,y}^{CO_2} - CT_{x,y}^{dry}}{\phi_{x,y}\left(CT_{CO_2} + 1000\right)} \quad \dots\dots\dots\dots\dots\dots\dots\dots\dots\dots\dots\dots\dots\dots\dots\dots\dots\dots\dots\dots \quad (4.3)$$

where:

$CT_{x,y}^{CO_2}$ is CT number of core saturated with CO_2 at x, y position.

$CT_{x,y}^{dry}$ is CT number of dry core at x, y position.

CT_{CO_2} is CT number of CO_2 used to calculate $CT_{x,y}^{CO_2}$.

$\phi_{x,y}$ is porosity at x, y position.

Fig 4.23 shows 3D saturation profile of supercritical CO_2 using 3D image processing software, *Petro3D* at CO_2 breakthrough in case of run 29 (2,700 psig, 80°C). We can see supercritical CO_2 just appear at outlet end. **Fig. 4.24** shows 3D saturation profile of supercritical CO_2 using 3D image processing software, *Petro3D* at the end of experiment in case of run 29. Only difference of CO2 saturation between Fig. **4.23** and Fig. **4.24** is shown at outlet end of core.
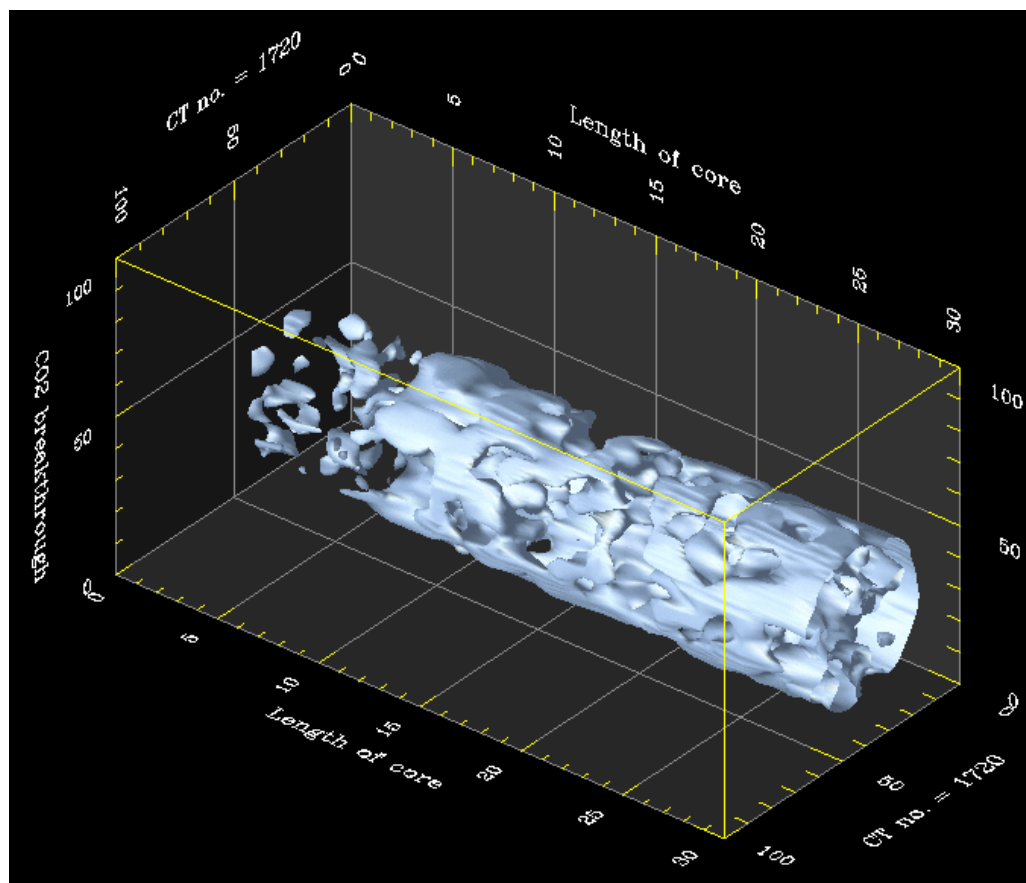
Fig. 4.23 – 3D saturation profile of supercritical CO$_2$ using 3D image processing software, *Petro3D* at CO$_2$ breakthrough in case of Run 29.
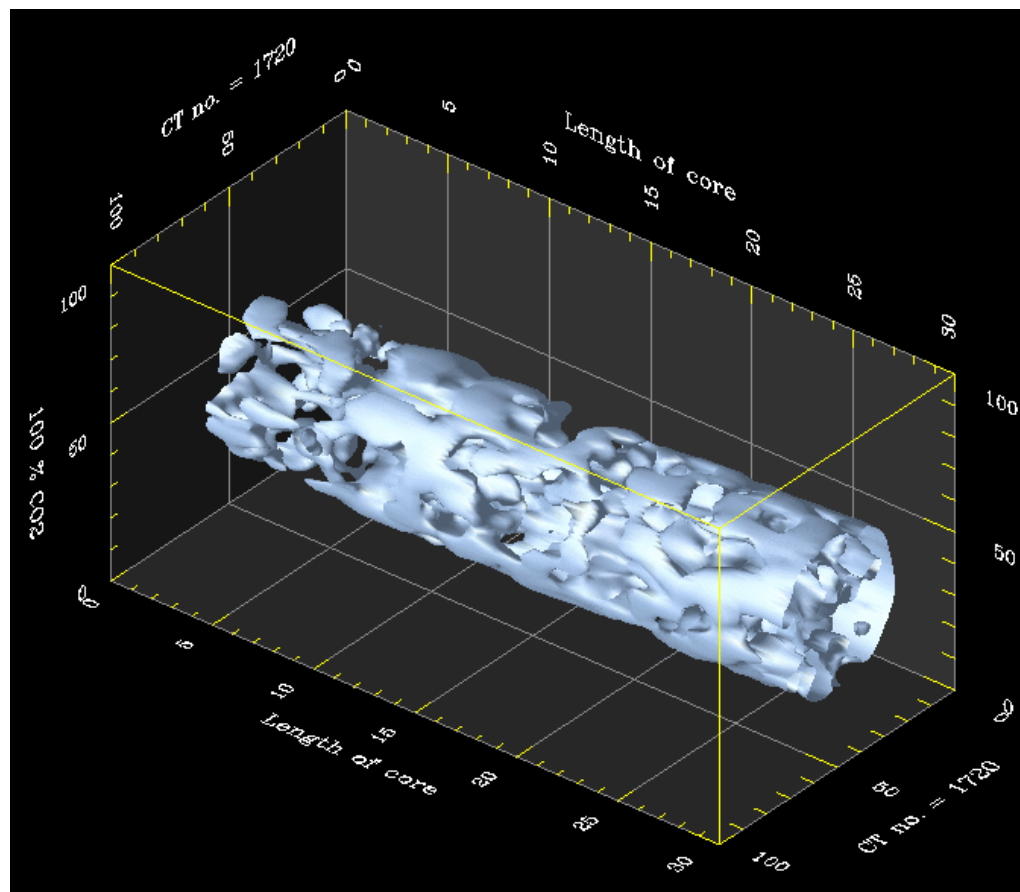
Fig. 4.24 – 3D saturation profile of supercritical CO₂ using 3D image processing software, *Petro3D* at the end of experiment in case of Run 29.

CHAPTER V

SIMULATION STUDY

5.1 Simulation Model

Carbon dioxide will behave as a supercritical fluid at pressures and temperatures typically encountered in the field. Supercritical fluids have liquid-like densities, gas-like diffusivities and could be liquid or gas dependent on pressure and temperature change in the field.

To conduct our simulation study we first determine gas-liquid relative permeability curves used in the field simulation study. In the experimental study, a carbonate core measuring 1 ft (30.5 cm) long and 1 in. (2.54 cm) in diameter is used. **Fig. 5.1** shows a 1D 96 grid-cell model used to represent the physical cell for history-matching the experimental results.

Fig. 5.2 shows history-matching with gas mass rate vs. time from experimental and simulation results for Run 21 (2,700 psig and 60°C).
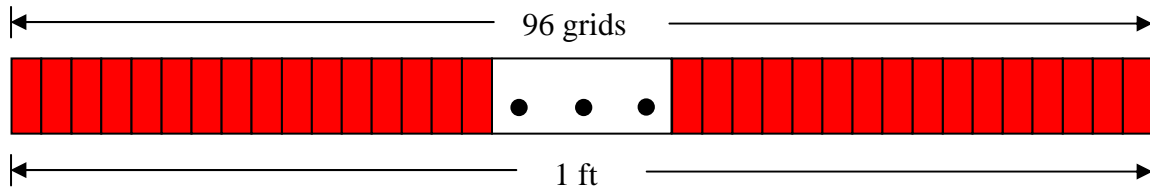
Fig. 5.1 – The 1D 96 grid-cell model to represent the physical cell.
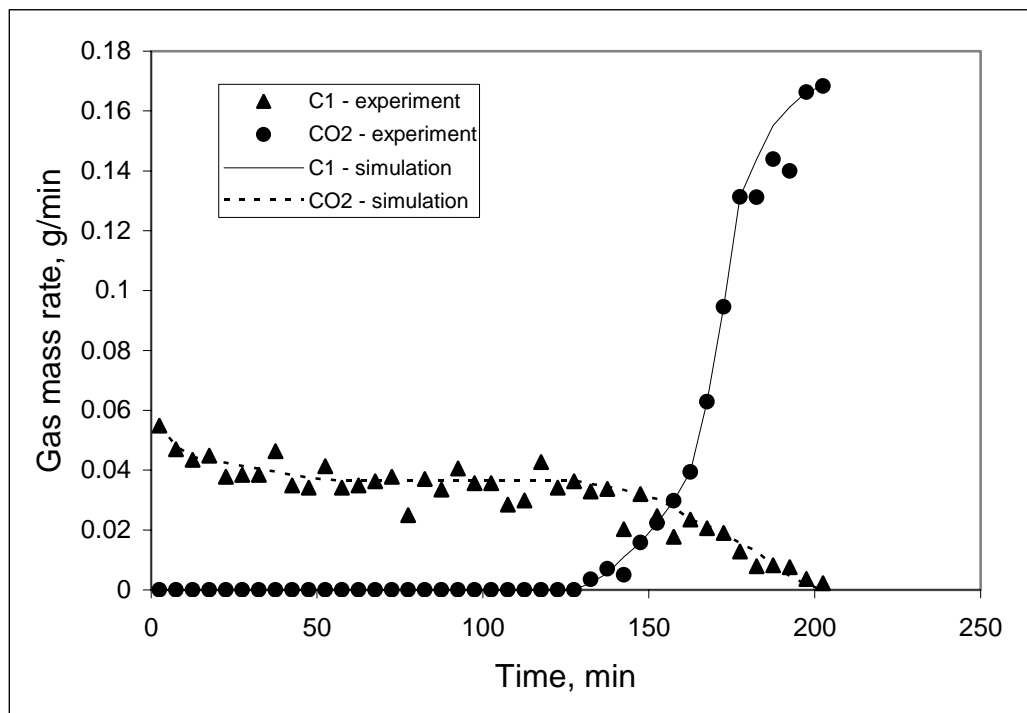
Fig. 5.2 – Gas mass rate vs. time from experimental and simulation results to calculate gas-liquid relative permeability curves.

Finally, the gas-liquid relative permeability curves are determined by history-matching the experimental results (**Fig. 5.3**).
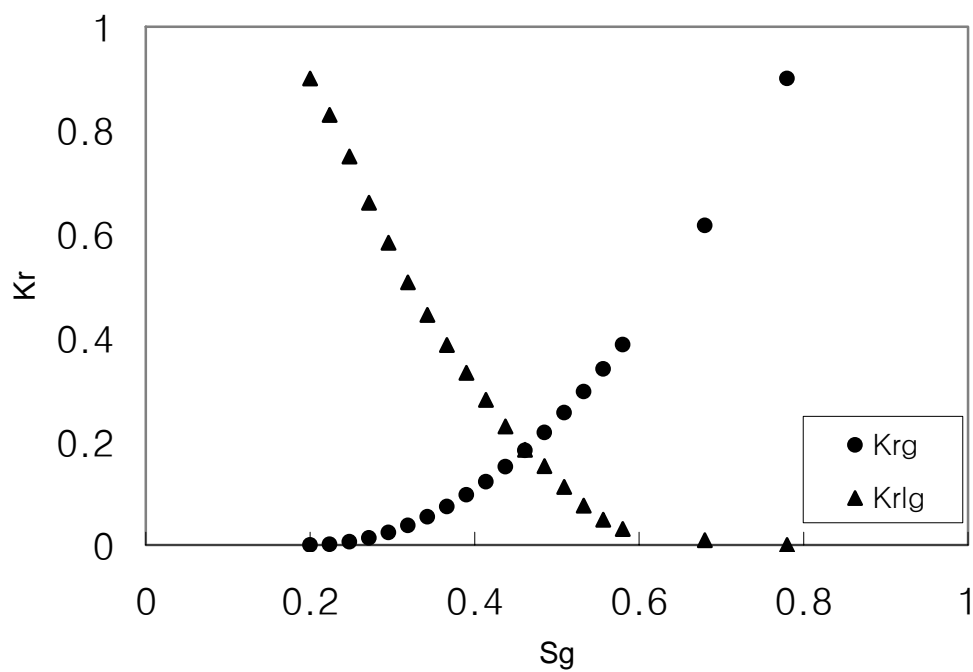
Fig. 5.3 – Gas-liquid relative permeability curves.

To simulate movable water in the gas reservoir, we also need CO_2-water relative permeability curves. I used Prieditis and Brugman's endpoint data for CO_2-water relative permeability curves (**Fig. 5.4**).[32]
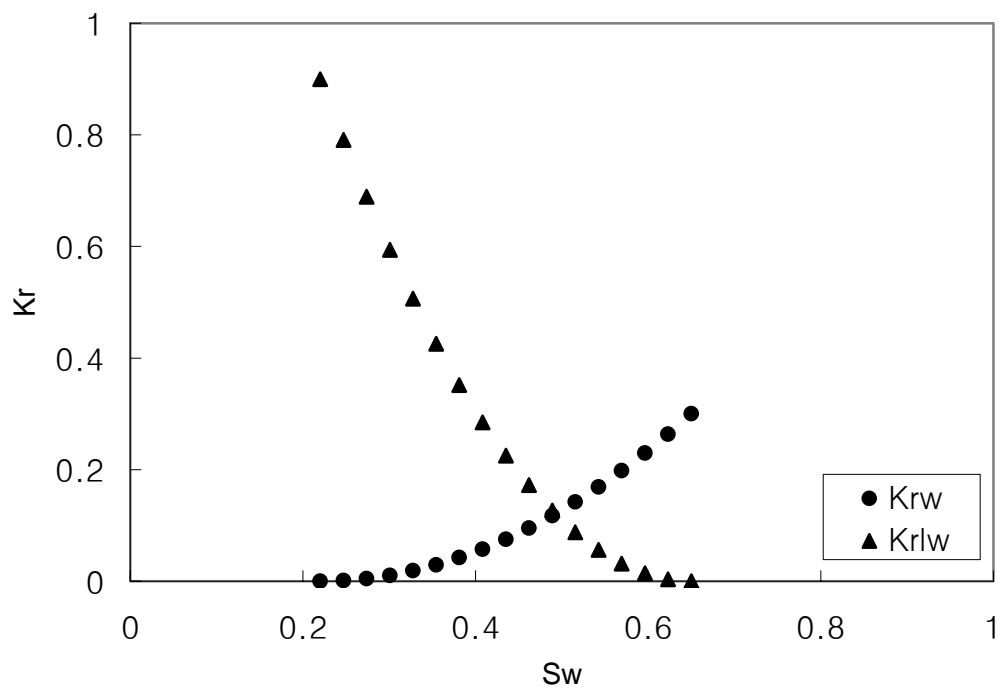
Fig. 5.4. – CO$_2$-water relative permeability curves.

A 3D simulation model of one eighth of a 5-spot pattern was constructed to simulate injection of supercritical CO_2 under two typical field conditions (**Table 5.1**).[33]

TABLE 5.1 – PROPERTIES OF TWO CASE SIMULATION MODELS

Property	Units	Case 1	Case 2
Five spot pattern area	acres	40	80
One eighth five spot area	acres	5	10
Thickness	ft	150	300
Layers	-	10	20
Pore volume	ft^3	7.5141E+06	3.00564E+07
Porosity	fraction	0.23	0.23
X, Y-direction permeability	md	50	50
Z-direction permeability	md	5	5
Initial water saturation	%	0, 25, 30, 35	0, 25, 30, 35
Temperature	°F	152	152
Original reservoir pressure	psia	3,045	3,045

Two pattern areas at a depth of 7000 ft were modeled, 40 acres (150 ft thickness: 15 ft × 10 layers), and 80 acres (300 ft thickness: 15 ft × 20 layers). To model fluid flow more accurately, smaller grids are made near the injector and producer than far from the wells and grids are parallel to the diagonal between the injector and producer (**Fig. 5.5**). The injector is perforated on the bottom most layer and the producer is perforated on the

top most layer. Injecting CO_2 at relatively deeper levels in a reservoir while producing from higher levels will allow an operator to decrease CO_2 upconing and mixing. Mixing is inhibited by the strong density contrast that causes CO_2 to fill the reservoir from the bottom up, making an effective vertical and lateral sweep.[34]
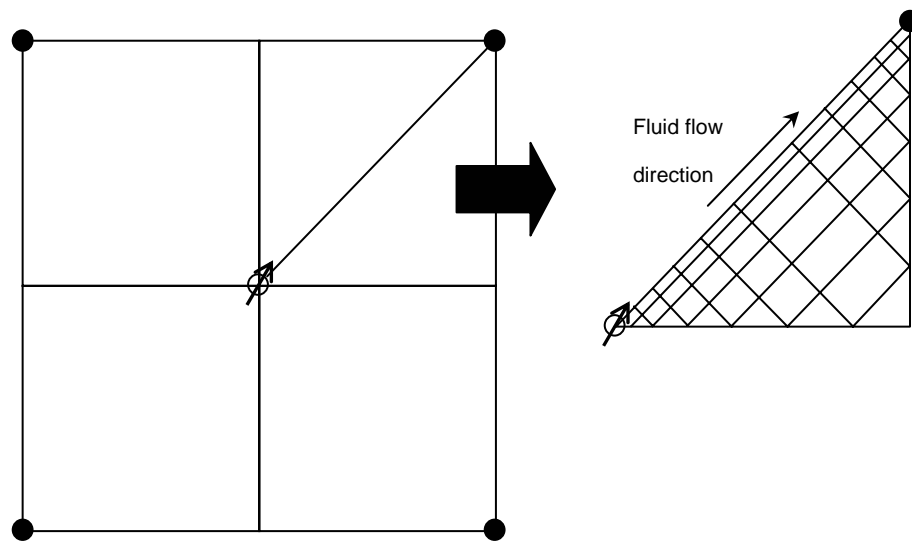
Fig. 5.5 – Schematic of one eighth of 5-spot and simulation model.

Porosity is 0.23 in both cases, which is calculated from CT scanner. We assumed x-direction permeability is same as y-direction permeability to 50 md, z-direction permeability is 5 md, and we considered initial water saturation as 0, 25, 30, and 35%.

Also, we assumed an original reservoir pressure of 3,045 psia from hydrostatic pressure gradient (0.435 psia/ft × 7000 ft). The reservoir temperature is taken as 152 °F from geothermal gradient (75 °F + 0.011 °F/ft × 7000 ft). Injection pressure of supercritical CO2 (3,245 psia) is 200 psia higher than original reservoir pressure (3,045 psia). When CO_2 is detected in the producer, we will shut in the producer and continue to inject supercritical CO_2 until field reaches the original reservoir pressure (3,045 psia). At this pressure, CO_2 injection into gas field will be terminated (**Fig. 5.6**).
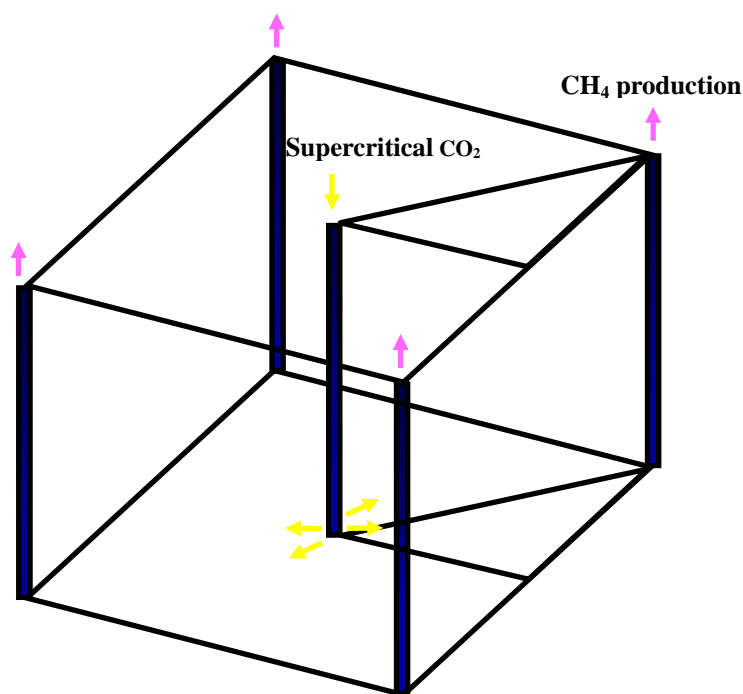
Fig. 5.6 – Schematic of the three-dimensional five spot.

5.2 Simulation Results

To evaluate the effect of injection rate and abandoned (initial) reservoir pressure on gas recovery factor, CO_2 breakthrough time, and the amount of CO_2 sequestered, we simulated two cases: case 1 (40 acres) and case 2 (80 acres).

First, for each case, we fixed abandoned (initial) reservoir pressure to 500 psia to find the effect of injection rate on recovery factor, breakthrough time, and the amount of CO_2 sequestered.

Fig. 5.7 shows methane recovery factor at CO_2 breakthrough for various injection rates of case 1 (40 acres) with different initial water saturation. Recovery factor is increased as injection rate is increased for each case. Recovery factor is low when water saturation is high at the same injection rate. Our results about methane recovery factor are similar to Clemens and Wit's results.[35]

Fig. 5.8 shows methane recovery factor at CO_2 breakthrough for various injection rates of case 2 (80 acres) with different initial water saturation. Recovery factor is increased as injection rate is increased at lower injection rates, but recovery factor is decreased preferably as injection rate increased at higher injection rates because CO_2 breakthrough occurred early without enough methane sweep. Recovery factor is increased as water saturation is decreased for each case.
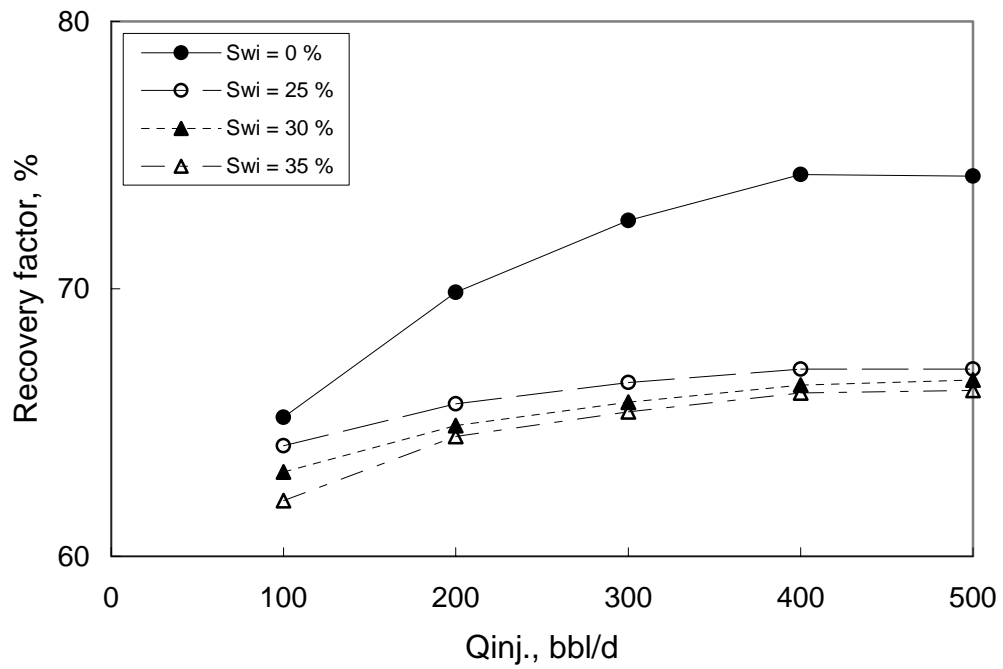
Fig. 5.7 – Methane recovery factor at CO$_2$ breakthrough for various injection rates of case 1 (40 acres).
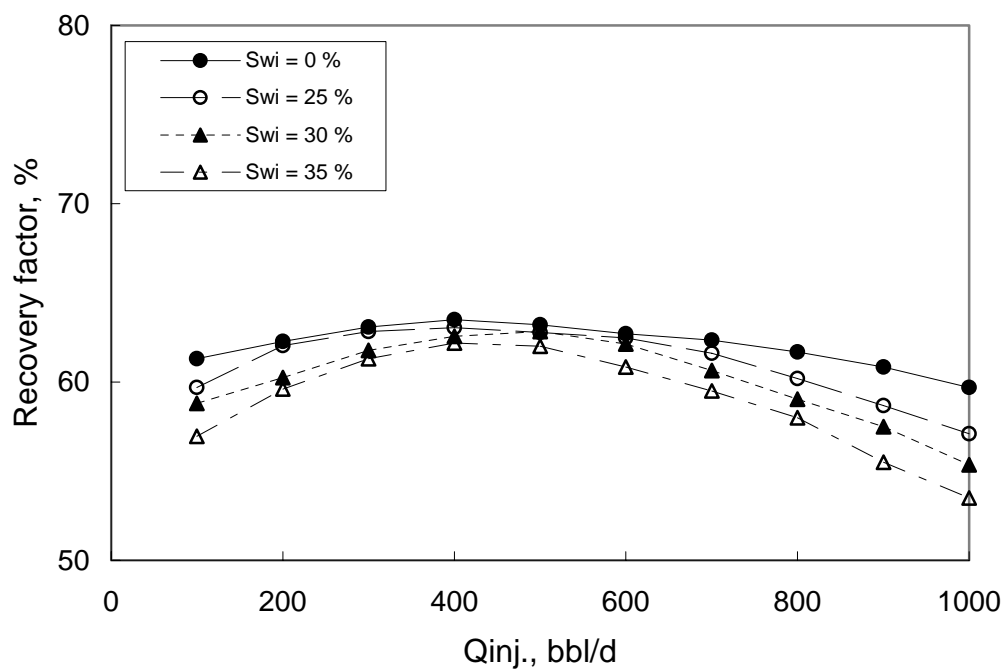
Fig. 5.8 – Methane recovery factor at CO_2 breakthrough for various injection rates of case 2 (80 acres).

Fig. 5.9 shows CO_2 breakthrough time vs. various injection rates in case 1. CO_2 breakthrough time is decreased exponentially as injection rate is increased and CO_2

breakthrough occurred early when water saturation is high. **Fig. 5.10** shows CO_2 breakthrough time vs. various injection rates in case 2.
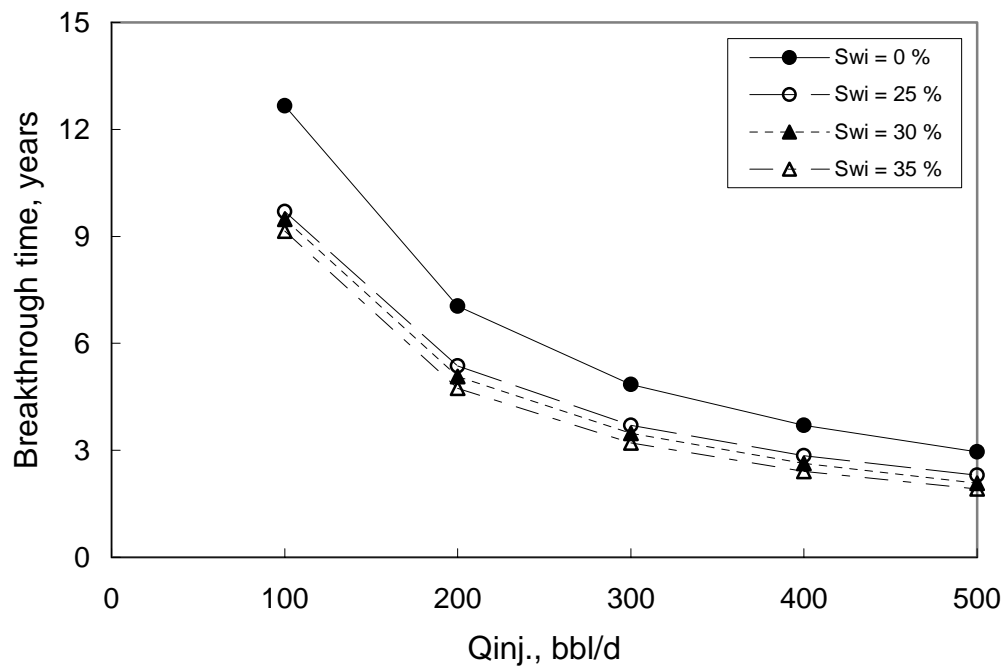
Fig. 5.9 – CO_2 breakthrough time for various injection rates in case 1 (40 acres).
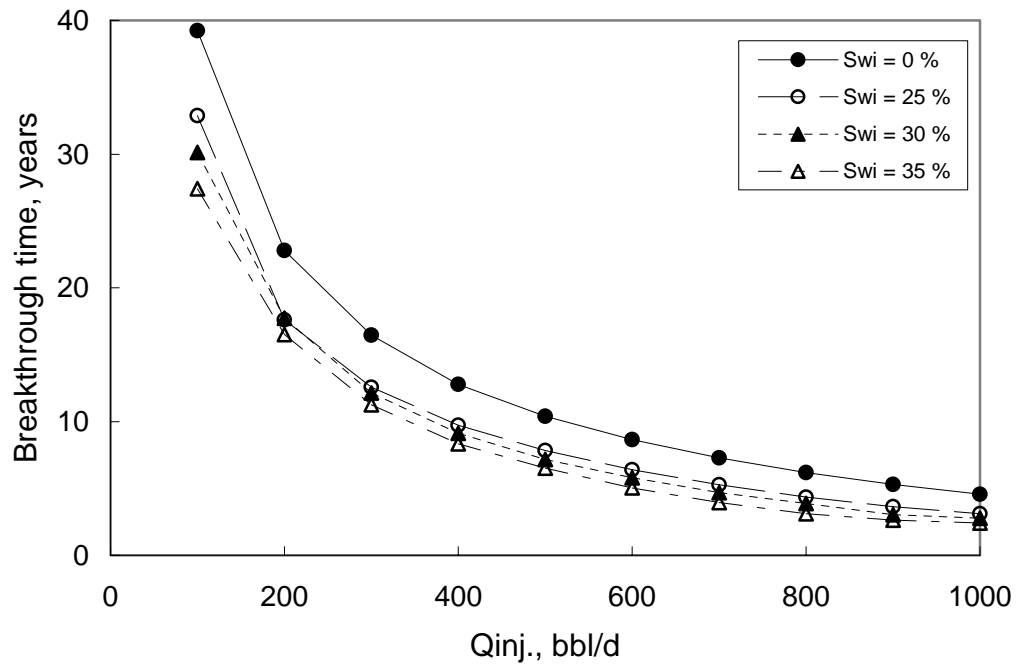
Fig. 5.10 – CO$_2$ breakthrough time for various injection rates in case 2 (80 acres).

The amounts of CO$_2$ sequestered in the gas field for different injection rates of case 1 and case 2 are shown in **Fig 5.11** and **Fig 5.12** respectively. The amounts of CO$_2$

sequestered are almost the same at same water saturation, independent of injection rate because the amounts of CO_2 sequestered are directly proportional to the pore volume.
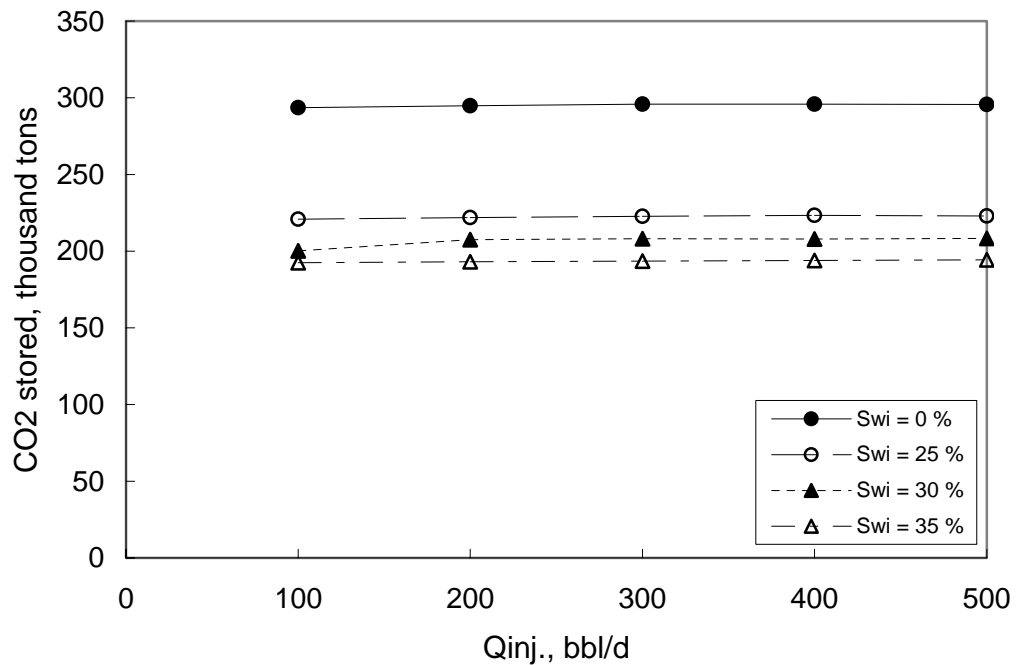
Fig. 5.11 – The amount of CO_2 sequestered for different injection rates in case 1 (40 acres).

Because the pore volume of case 2 is 4 times bigger than that of case 1, the amount of CO_2 sequestered in case 1 is exactly 4 times bigger than that of case 1.
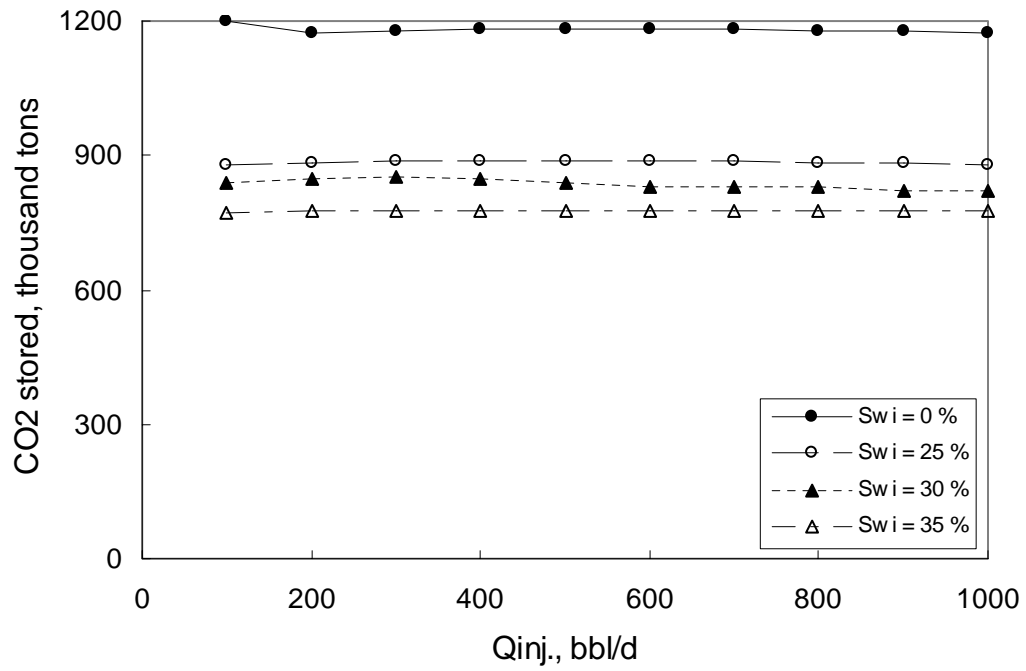
Fig. 5.12 – The amount of CO₂ sequestered for different injection rates in case 2 (80 acres).

At lower injection rate, time of injection end is longer.   This relationship is shown in **Fig. 5.13** and **Fig. 5.14**.
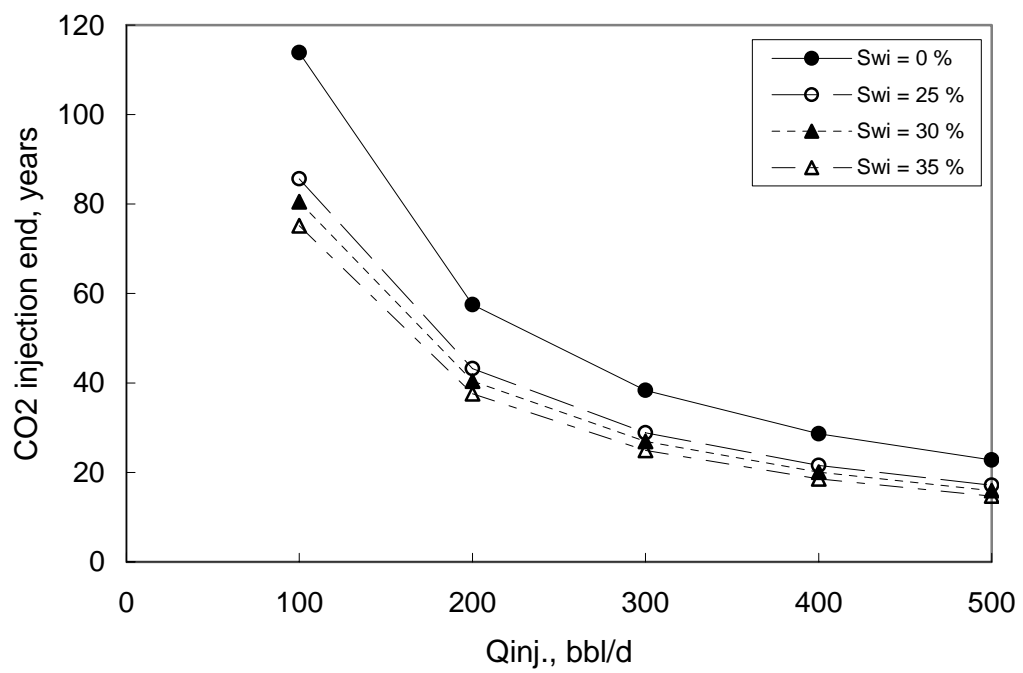
Fig. 5.13 – CO₂ injection end for various injection rates of case 1 (40 acres).
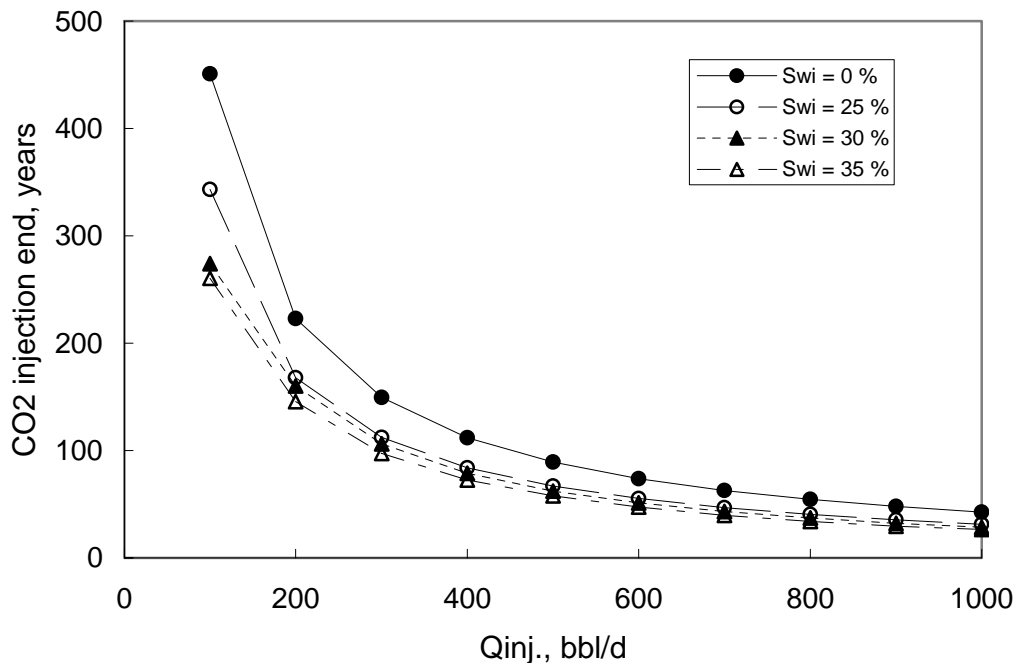
Fig. 5.14 – CO$_2$ injection end for various injection rates of case 2 (80 acres).

Using the procedure given above, we found the optimum injection rate to maximize both recovery factor and the amount of CO$_2$ sequestered. To find the effect of abandoned (initial) reservoir pressure on recovery factor, breakthrough time, and the amount of CO$_2$ sequestered, we simulated the two cases with fixed injection rate (400 b/d).

Fig. 5.15 and **Fig. 5.16** show recovery factor at various abandoned reservoir pressures with different initial water saturation for case 1 and case 2 respectively. Recovery factor is decreased as abandoned reservoir pressure is increased and recovery

factor is low when water saturation is high at the same abandoned reservoir pressure because CO_2 breakthrough occurred earlier as initial water saturation is higher. The recovery factor in the more depleted and smaller gas field is bigger.
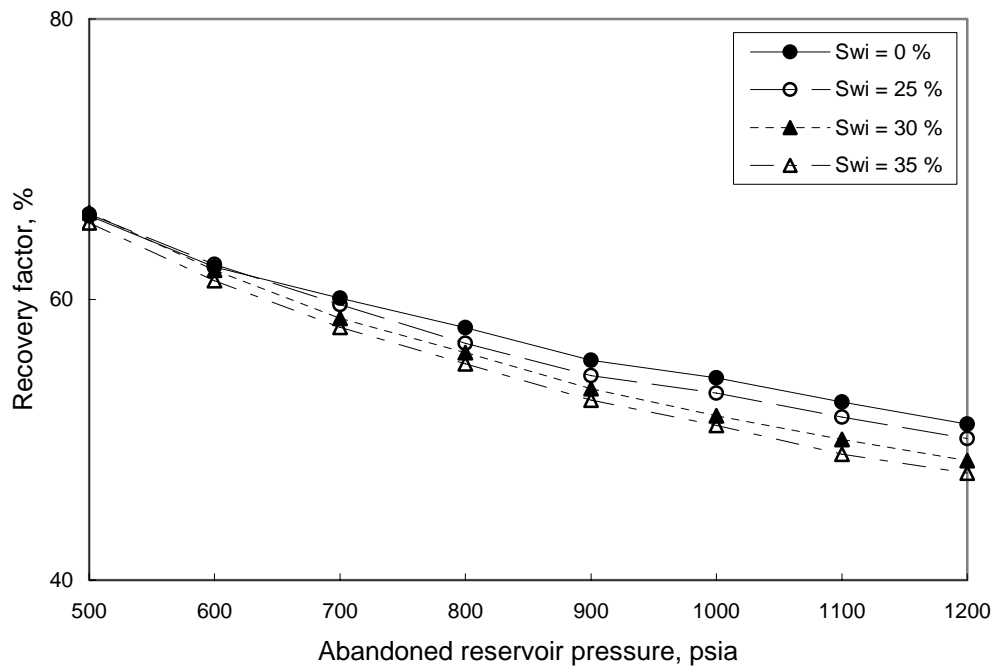
Fig. 5.15 – Methane recovery factor at CO_2 breakthrough for various abandoned reservoir pressure in case 1 (40 acres).
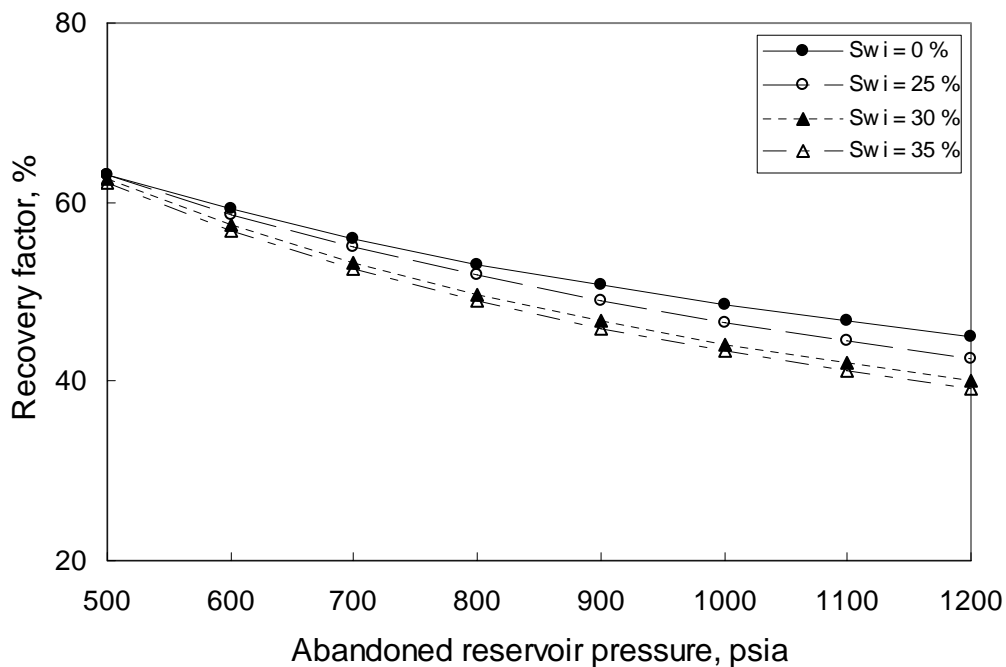
Fig. 5.16 – Methane recovery factor at CO_2 breakthrough for various abandoned reservoir pressure in case 2 (80 acres).

CO$_2$ breakthrough time versus abandoned reservoir pressures with different water saturation for case 1 is shown in **Fig. 5.17**. CO_2 breakthrough time is decreased as abandoned reservoir pressure is increased at each initial water saturation and CO_2 breakthrough occurred early when water saturation is high. **Fig. 5.18** shows CO_2 breakthrough time vs. various injection rates in case 2.
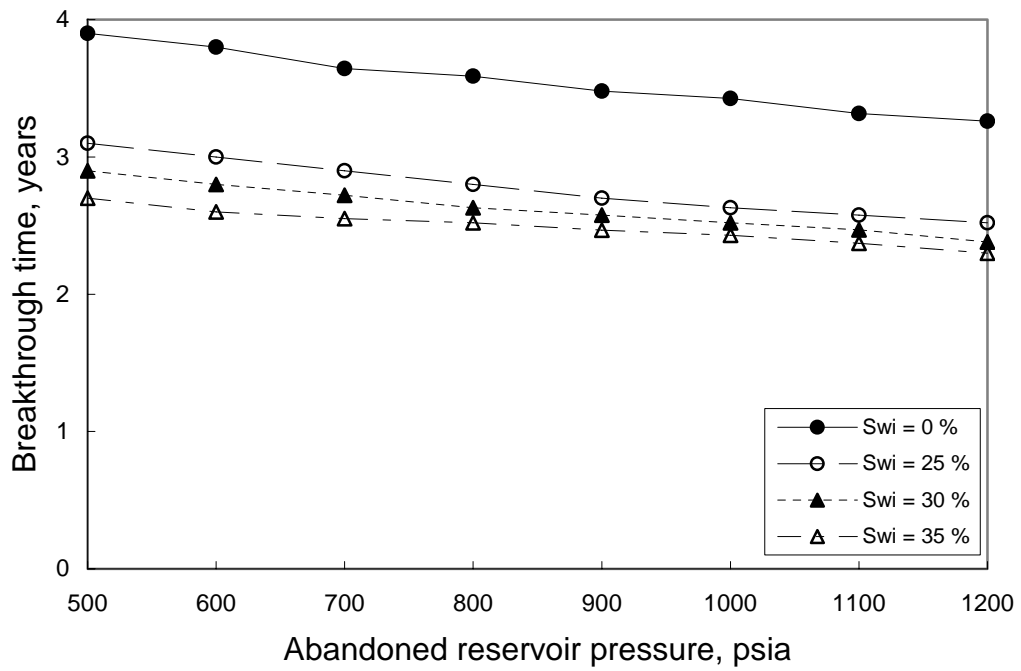
Fig. 5.17 – CO₂ breakthrough time vs. abandoned reservoir pressures with different water saturation in case 1 (40 acres).
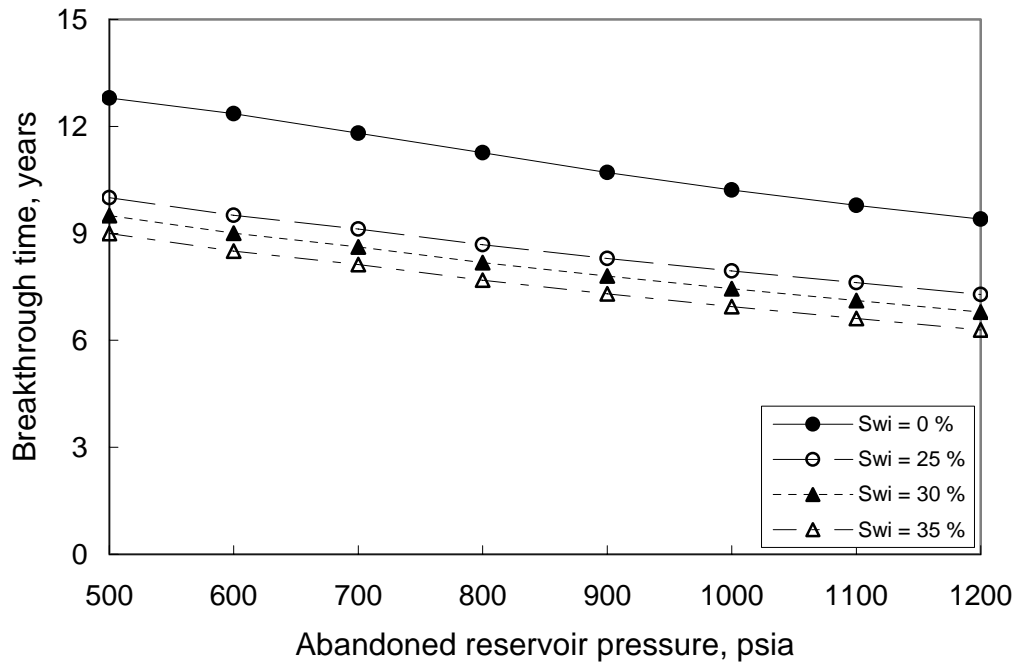
Fig. 5.18 – CO₂ breakthrough time vs. abandoned reservoir pressures with different water saturation in case 2 (80 acres).

Fig. 5.19 and **Fig. 5.20** show the relationship between the amounts of CO_2 sequestered and abandoned reservoir pressures of case 1 and case 2 respectively. The amount of CO_2 sequestered in more depleted at each initial water saturation and larger gas reservoir is bigger because the amounts of CO_2 sequestered are directly proportional to the pore volume.
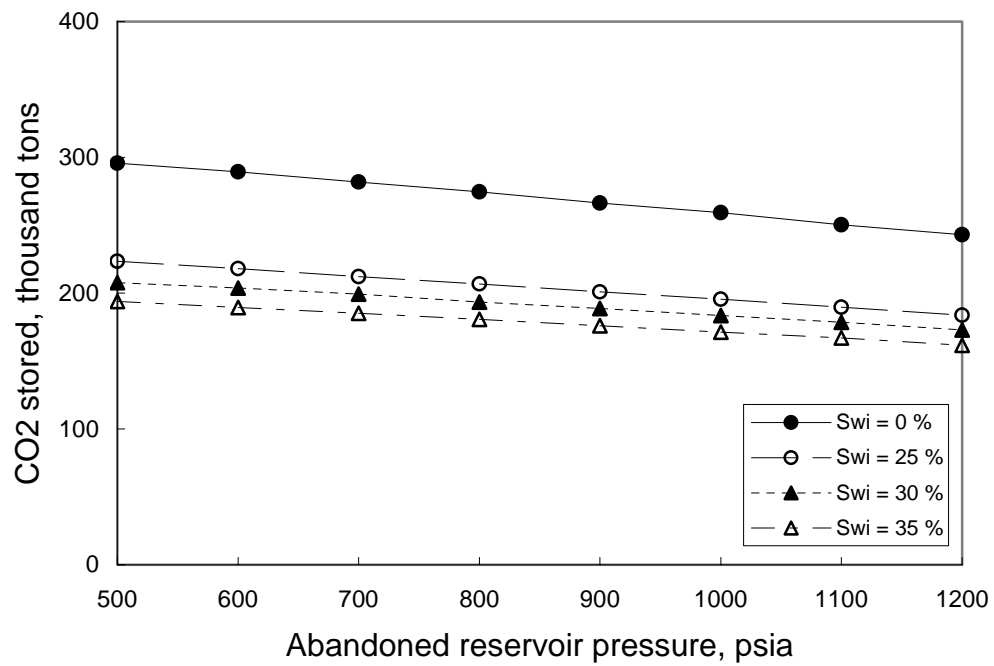
Fig. 5.19 – The amount of CO₂ sequestered for various abandoned reservoir pressure in case 1 (40 acres).
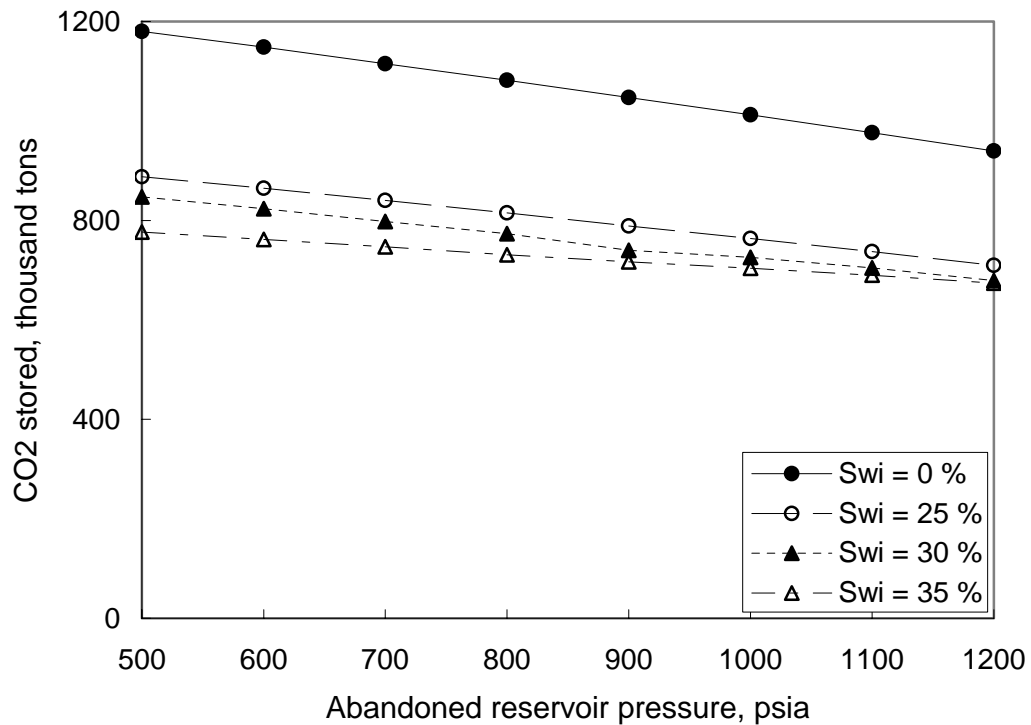
Fig. 5.20 – The amount of CO₂ sequestered for various abandoned reservoir pressure in case 2 (80 acres).

At lower abandoned reservoir pressure for each initial water saturation, time of injection end is longer.   **Fig. 5.21** and **Fig. 5.22** show this relationship.
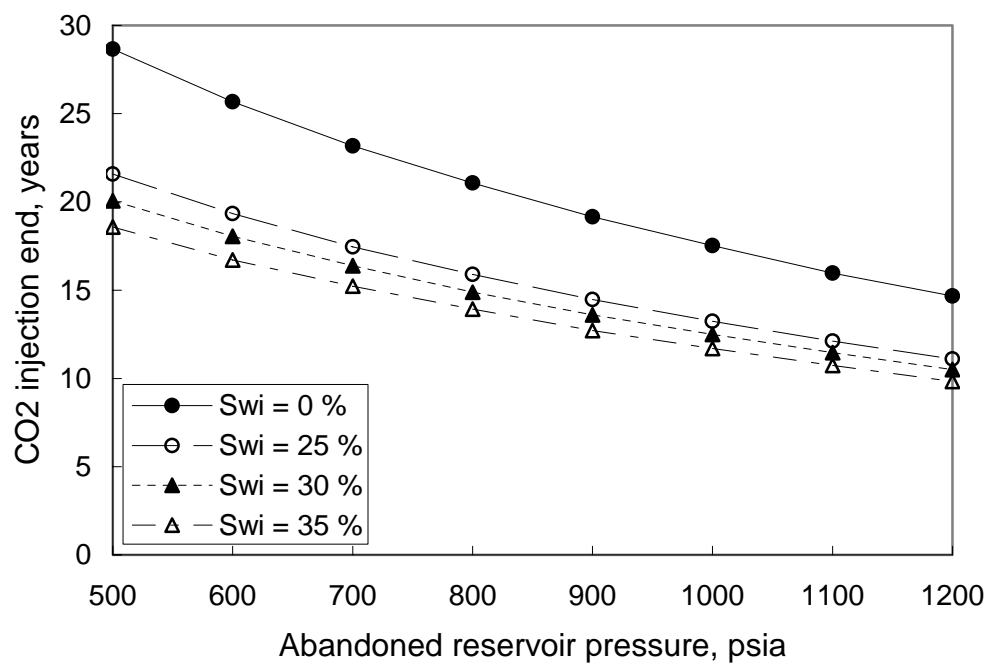
Fig. 5.21 – CO₂ injection end for various abandoned reservoir pressure in case 1 (40 acres).
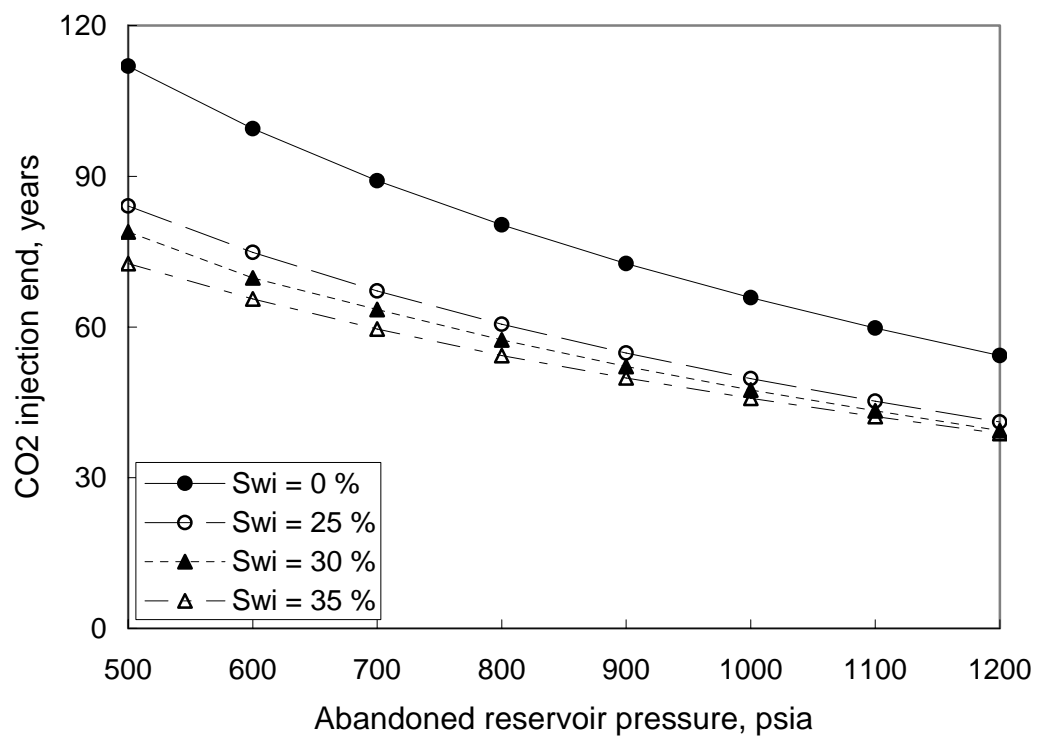
Fig. 5.22 – CO₂ injection end for various abandoned reservoir pressure in case 2 (80 acres).

CHAPTER VI

SUMMARY, CONCLUSIONS, AND RECOMMENDATIONS

6.1 Summary

The primary objective of this research is to investigate the feasibility of sequestering supercritical carbon dioxide in gas-bearing carbonate reservoirs. Experiments were conducted in which supercritical carbon dioxide was injected into a cell containing methane. Porosity of carbonate core and fluid saturation were measured with the aid of an x-ray CT scanner. The convection-dispersion equation was used to determine the coefficient of dispersion of supercritical carbon dioxide in gas-bearing carbonate reservoirs.

The main findings and conclusions from this study are summarized as follows.

6.2 Conclusions

Experimental results may be summarized as follows.

1. For the 1 ft long $\times$ 1 in. diameter core used in the experiments, CO_2 breakthrough time for 0.25 cc/min injection was 145 min.
2. Methane recovery at breakthrough time ranged from 62 % to 87 % of initial gas in-place in the core.

3. Displacement of methane by CO_2 – whether CO_2 is a gas, liquid, or a supercritical fluid – appears to be a very efficient process. Dispersion coefficient of CO_2 in methane is relatively low, 0.01-0.3 cm^2/min.

4. For the same temperature, coefficient of longitudinal dispersion of CO_2 decreases with increasing pressure. This is due to the fact that CO_2 becomes more "liquid like" at higher pressure. For example, at 60°C, coefficient of longitudinal dispersion decreases from 0.2 cm^2/min at 1,200 psig to 0.04 cm^2/min at 2,700 psig.

5. At constant pressure, with increase in temperature, coefficient of longitudinal dispersion of CO_2 increases, due to CO_2 becoming more "gas like". For example, at 2,700 psig, coefficient of longitudinal dispersion increases from 0.021 cm^2/min at 40°C to 0.07 cm^2/min at 80°C.

Reservoir simulation of one-eighth of 5-spot patterns gave the following main results.

1. A large amount of CO_2 is sequestered: 1.2 million tons in 29 years (0 % initial water saturation), 0.9 million tons in 22 years (25 % initial water saturation), 0.83 million tons in 20 years (30 % initial water saturation), and 0.78 million tons in 19 years (35 % initial water saturation) for 40-acres pattern, and 4.8 million tons in 112 years (0 % initial water saturation), 3.6 million tons in 84 years (25 % initial water saturation), 3.4 million tons in 79 years (30 % initial water saturation), and 3.1 million tons in 73 years (35 % initial water saturation) for 80-acres pattern. The

amounts of CO_2 sequestered in more depleted and larger gas reservoir are larger. However, injection rate does not affect the amounts of CO_2 sequestered.

2.   A significant amount of a natural gas is also produced.   For a 40-acres pattern, natural gas production amounts to 1.2 BSCF or 74 % remaining GIP (0 % initial water saturation), 0.9 BSCF or 67 % remaining GIP (25 % initial water saturation), 0.84 BSCF or 66.4 % remaining GIP (30 % initial water saturation), and 0.78 BSCF or 66.1 % remaining GIP (35 % initial water saturation).   For a 80-acres pattern, natural gas production amounts to 4.5 BSCF or 63.5 % remaining GIP (0 % initial water saturation), 3.41 BSCF or 63 % remaining GIP (25 % initial water saturation), 3.2 BSCF or 62.6 % remaining GIP (30 % initial water saturation), and 2.97 BSCF or 62.2 % remaining GIP (35 % initial water saturation).

3.   At \$2.00/MSCF, produced gas revenue amounts to \$2.4 million (0 % initial water saturation) to \$1.56 million (35 % initial water saturation) for 40-acre pattern and \$9 million (0 % initial water saturation) to \$5.94 million (35 % initial water saturation) for 80-acre pattern, which could help defray the cost of CO_2 sequestration.   In short, CO_2 sequestration in depleted gas reservoirs appears to be a win-win technology.

6.3 Recommendations

1. This experimental study has been restricted to one-dimensional horizontal displacement of C_1 by CO_2.   In practice, gravity segregation would increase

displacement stability and thus help recovery of natural gas during sequestration of CO_2. A 3D experimental study of CO_2 sequestration is therefore recommended to study the effect of gravity segregation.

2. This study has been performed using a carbonate core. Similar studies using sandstone cores are recommended.

3. In practice, "impurities" such as CO, SO_2, NOx, etc are present in flue gas to be sequestered. Effect of these "impurities" on CO_2 displacement efficiency needs to be investigated.

NOMENCLATURE

K_l = coefficient of longitudinal dispersion

C = concentration of supercritical carbon dioxide at time t and location x

C_R = reaction rate concentration of supercritical carbon dioxide with the reservoir

v = interstitial velocity of supercritical carbon dioxide $(= Q / \pi \, r^2 \, \phi)$

Q = flow rate

R = radius of core

ϕ = core porosity

x_D = dimensionless distance

L = length of core

t_D = dimensionless time

Pe = Peclet number

$\phi_{x,y}$ = porosity at x, y position

$S_{x,y}^{sample}$ = saturation at x, y position

$CT_{x,y}^{100\% \, Water}$ = CT number of core saturated with 100 % water at x, y position

$CT_{x,y}^{dry}$ = CT number of dry core at x, y position

CT_{water} = CT number of water used to calculate $CT_{x,y}^{100\% \, Water}$

$CT_{x,y}^{100\% \, Sample}$ = CT number of core saturated with sample at x, y position

CT_{sample} = CT number of sample used to calculate $CT_{x,y}^{100\% \, Sample}$

S_g = gas saturation

K_{rg} = relative permeability to gas

K_{rlg} = relative permeability to liquid

S_w = water saturation

K_{rw} = relative permeability to water

S_{wi} = initial water saturation

Q_{inj} = injection rate

REFERENCES

1. Abrardo, J.M., Aminian, K., Ahnell, A.D., Anderson, C.W., and Allmaras, R.R.: "Carbon Sequestration," final report, U.S. DOE, Gaithersburg, Maryland (December 1999).

2. Thambimuthu, K.V., McMullan, P., Wright, J., Wilson, M., and Seckington, B.: "Capture & Storage of CO_2," annual report, IEA GHG, Stoke Orchard, United Kingdom (November 2002).

3. Herzog, H., Eliasson, B., and Kaarstad, O.: "Capturing Greenhouse Gases," *Scientific American* (February 2000) 72-79.

4. Medina, M.G., Bond, G.M., and Stringer J.: "An Overview of Carbon Dioxide Sequestration," *The Elecrochemical Society Interface* (Spring 2001) 26-30.

5. Stevens, S.H., Kuuskraa, V.A., Spector, D., and Riemer, P.: "CO_2 sequestration in Deep Coal Seams: Pilot Results and Worldwide Potential," presented at the 1998 Fourth International Conference on Greenhouse Gas Control Technologies, Interlaken, Switzland, 30 August-2 September.

6. Tek, M.R.: "Underground Storage of Natural Gas: Theory and Practice," In: NATO ASI Series E, Applied Sciences, Kluwer, Boston, MA (1989) **171**, 458.

7. Bradley, R.A., Watts, E.C., and Williams, E.R.: *Limiting Net Greenhouse Gas Emissions in the US*, report to the US Congress, U.S. DOE, Washington, DC (1991).

8. Crossley, N.G.: "Conversion of LPG salt caverns to natural gas storage - A Transgas experience," *Journal of Canadian Petroleum Technology* (1998) **12**, 37-47.

9. Bachu, S.: "Sequestration of CO_2 in Geological Media: Criteria and Approach for Site Selection in Response to Climate Change," *Energy Conversion & Management* (2000) **41**, 953-970.

10. Yamaguchi, S.: "A Fundamental Numerical Study on CO_2 injection into Aquifers," *Int. J. of The Soc. of Mat. Eng. for Resources* (1999) **7**, 44-54.

11. Pruess, K., Xu, T., Apps, J., and Garcia, J.: "Numerical Modeling of Aquifer Disposal of CO_2," *SPEJ* (March 2003) 49-60.

12. Korbul, R. and Kaddour, A.: "Sleipner Vest CO_2 Disposal - Injection of Removed CO_2 into the Utsira Formation," *Energy Conversion and Management* (1995) **36**, 509-512.

13. Holloway, S.: "An Overview of the Joule II Project 'The Underground Disposal of Carbon Dioxide," *Energy Conversion and Management* (1996) **37**, 1149-1154.

14. Holloway, S. and van der Straaten, R.: "The Joule II Project - The Underground Disposal of Carbon Dioxide," *Energy Conversion and Management* (1995) **36**, 519-522.

15. Pearce, J.M., Holloway, S., Wacker, H., Nelis, M.K., Rochelle, C., and Bateman, K.: "Natural Occurrences as Analogues for the Geological Disposal of Carbon Dioxide," *Energy Conversion and Management* (1996) **37**, 1123-1128.

16. AGA (American Gas Association) committee on underground storage, Task Group on Statistics, 29th Annual Report on Statistics, XU0578, Arlington, VA (1979) 51.

17. Katz, D.L. and Tek, M.R.: "Overview of Underground Storage of Natural Gas," *JPT* (June 1981) 731.

18. Stevens, S.H. and Riemer, P.: "Enhanced Coalbed Methane Recovery Using CO_2 Injection: Worldwide Resource and CO_2 Sequestration Potential," paper SPE 48881 presented at the 1998 SPE International Conference and Exhibition, Beijing, China, 2-6 November.

19. Stalkup, F.I.: *Miscible Displacement*. Monograph Series, SPE, Richardson, TX (1984) **1**, 13-16.

20. Krishnan, A., Zhou, N., and Giridharan, M.G.: "Transport Phenomena in Supercritical Fluids," Paper AIAA 95-2233, presented at the 1995 AIAA Fluid Dynamic Conference, San Diego, California, 19-22 July.

21. Hagoort, J.: *Fundamental of Gas Reservoir Engineering*, Elsevier Science Publishers, New York (1988).

22. Abramowitz, M. and Stegun, I.A.: *Handbook of Mathematical Functions*. Dover Publications Inc., New York (1972).

23. Mamora, D.D. and Seo, J.G.: "Enhanced Gas Recovery by Carbon Dioxide Sequestration in Depleted Gas Reservoirs," paper SPE 77347 presented at the 2002 SPE Annual Technical Conferences and Exhibition, San Antonio, Texas, 29 September-2 October.

24. Wellington, S.L. and Vineger, H.J.: "X-Ray Computed Tomography," *JPT* (August 1987) 885-898.

25. Angulo, R. and Ortiz, N.: "X-Ray Tomography Application in Porous Media Evaluation," paper SPE 23670 presented at the 1992 second Latin American Petroleum Engineering Conference II LAPEC, Caracas, Venezuels, 8-11 March.

26. Honarpour, M.M., Cromwell, V., Hatton, D., and Satchwell, R.: "Reservoir Rock Descriptions Using Computed Tomography (CT)," paper SPE 14272 presented at the 1985 SPE Annual Technical Conference and Exhibition, Las Vegas, Nevada, 22-25 September.

27. Cromwell, V., Kortum, D.J., and Bradley, D.J.: "The Use of a Medical Computer Tomography (CT) System to Observe Multiphase Flow in Porous Media," paper SPE 13098 presented at the 1984 SPE Annual Technical Conference and Exhibition, Houston, Texas, 16-19 September.

28. Gilliland, R.E., and Coles, M.E.: "Use of CT Scanning in the Investigation of Damage to Unconsolidated Cores," paper SPE 19408 presented at the 1990 SPE Formation Damage Control Symposium, Lafayette, Louisiana, 22-23 February.

29. Mellon, M.G.: *Analytical Absorption Spectroscopy*, John Wiley and Sons, New York (1950) Ch. 2, 90-95.

30. Evans: *The Atomic Nucleus*, McGraw-Hill Book Co., New York (1955).

31. Withjack, E.M.: "Computed Tomography for Rock-Property Determination and Fluid-Flow Visualization," paper SPE 16951 presented at the 1987 SPE Annual Technical Conference and Exhibition, Dallas, Texas, 27-30 September.

32. Prieditis, J. and Brugman, R.J.: "Effects of Recent Relative Permeability Data on CO_2 Flood Modeling," paper SPE 26650 presented at the 1993 SPE Annual Technical Conference and Exhibition, Houston, Texas, 3-6 October.

33. Seo, J.G., and Mamora, D.D.: "Experimental and Simulation Studies of Sequestration of Supercritical Carbon Dioxide in Depleted Gas Reservoirs," paper

SPE 82100 presented at the 2003 SPE/EPA/DOE Exploration & Production Environmental Conference, San Antonio, 10-12 March.

34. Oldenburg, C.M. and Benson, S.M.: "CO_2 Injection for Enhanced Gas Production and Carbon Sequestration," paper SPE 74367 presented at the 2002 SPE International Petroleum Conference and Exhibition, Villahermosa, Mexico, 10-12 February.

35. Clemens, T.G. and Wit, K.: "CO_2 Enhanced Gas Recovery Studies for an Example Gas Reservoir," paper SPE 77348 presented at the 2002 SPE Annual Technical Conferences and Exhibition, San Antonio, Texas, 29 September-2 October.

36. Kreyszig, E.: *Advanced Engineering Mathematics*, John Wiley and Sons, New York (1993).

APPENDIX A

COMPUTER PROGRAMS

The computer program to calculate dispersion coefficient is listed in this appendix.

Program	Main Function
1. DC.FOR	Compute dispersion coefficient.
2. DC.DAT	Input data (length of core, flow rate, radius of core, and porosity).

1. DC.FOR

```
C      **************************************************
C             COMPUTE THE DISPERSION COEFFICIENT
C      **************************************************
       IMPLICIT REAL (A-H,O-Z)
       OPEN (UNIT=1,FILE='DC.DAT',STATUS='UNKNOWN')
       OPEN (UNIT=2,FILE='DC.OUT',STATUS='UNKNOWN')
       READ (1,*)
       READ (1,*) CL
   READ (1,*)
       READ (1,*) Q
   READ (1,*)
       READ (1,*) R
       READ (1,*)
       READ (1,*) PHI
C      **************************************************
       DATA A1,A2,A3/0.254829592,-0.284496736,1.421413741/
       DATA A4,A5/-1.453152027,1.061405429/

       DC=0.15
   XD=1.0
C      **************************************************
   DO 30 TIME=0.000001,110.0,1.0
       V=Q/(3.14*(R**2)*PHI)
```

```
        TD=(TIME*V)/CL
        PE=(V*CL)/DC

        Y1=(XD-TD)/(2.0*SQRT(TD/PE))
        Y2=(XD+TD)/(2.0*SQRT(TD/PE))


         Z2=1.0/(1.0+0.3275911*Y2)

             IF (Y1.LT.0.0) THEN
        Y1=-Y1
             Z1=1.0/(1.0+0.3275911*Y1)
        EC1=2-(A1*Z1+A2*Z1**2+A3*Z1**3+A4*Z1**4+A5*Z1**5)
          *EXP(-Y1**2)
        Y1=-Y1
        ELSE
                 Z1=1.0/(1.0+0.3275911*Y1)
               EC1=(A1*Z1+A2*Z1**2+A3*Z1**3+A4*Z1**4+A5*Z1**5)
           *EXP(-Y1**2)
         ENDIF
        EC2=(A1*Z2+A2*Z2**2+A3*Z2**3+A4*Z2**4+A5*Z2**5)*EXP(-Y2**2)

        C=(1.0/2.0)*(EC1+EXP(PE*XD)*EC2)
      CC=C*100

        WRITE (2,*) TIME, CC
30        CONTINUE
C20     CONTINUE
C10     CONTINUE
      CLOSE(1)
      CLOSE(2)
      STOP
      END
```

2. DC.DAT

```
[LENGTH OF CORE, CM]
30.48
[FLOW RATE, CC/MIN]
0.25
[RADIUS OF CORE, CM]
1.27
[POROSITY]
0.23
```

APPENDIX B

CONVECTION-DISPERSION EQUATION

<u>Continuity Equation</u>

Suppose we have a control volume V which is bound by a surface S. Control volume is an open system, ie, matter can cross the boundary. This is different from a material volume (control mass) which is closed. We want to express the conservation of source quantity A (mass, momentum, energy, electric charge, etc.).
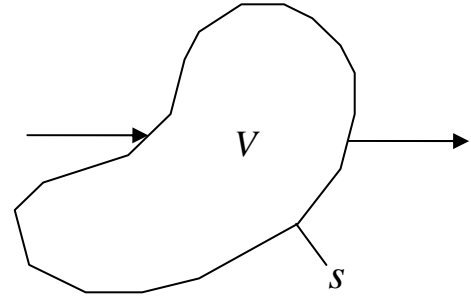
Let's consider a differential volume, dV

$$\begin{bmatrix} Rate\ of\ increase \\ of\ A\ in\ V \end{bmatrix} = \begin{bmatrix} Rate\ of\ Inflow \\ of\ A\ in\ V \end{bmatrix} - \begin{bmatrix} Rate\ of\ outflow \\ of\ A\ in\ V \end{bmatrix} + \begin{bmatrix} Rate\ of\ creation \\ of\ A\ in\ V \end{bmatrix}^{0}$$

"Accumulation Term"

$$= \begin{bmatrix} Net\ rate\ of\ Inflow \\ of\ A\ in\ V \end{bmatrix}$$

"Convective Term"

If we consider a porous medium with porosity, ϕ, saturated by oil and water (S_o, S_w) with densities (ρ_o, ρ_w) moving with velocities, $\vec{V_o}$ and $\vec{V_w}$, then we can express the mass conservation of the oil phase.

Accumulation Term

$$\frac{d}{dt} \int_V \rho_o \ S_o \phi \ dV$$

Convective Term

Let's break up S into many small dS
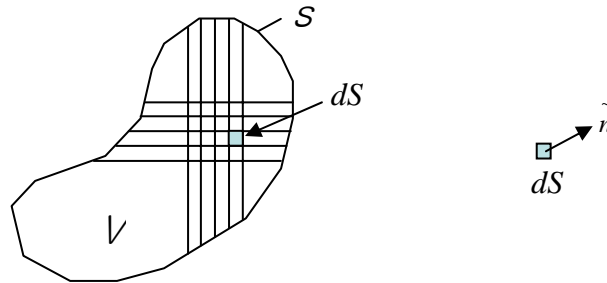
We represent the orientation of dS by $\tilde{n}$ which is an outwardly directed unit normal vector.

Side view of dS
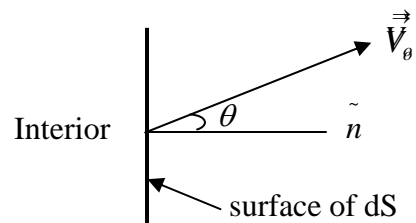
Component of $\vec{V_o}$ which crosses the surface is

$$\vec{V_\perp} \ = \ \tilde{n} \bullet \vec{V_o} \ = \ \left|\vec{n}\right| \left|\vec{V_o}\right| \ \cos\theta \ = \ \left|\vec{V_o}\right| \ \cos\theta$$

Convective Term

$$- \int_S \tilde{n} \cdot \rho_o \, \vec{V}_o \, dS$$

Let's consider multicomponent multiphase flow, from the conservation principle

$$\begin{bmatrix} Rate \ of \ increase \\ of \ A \ in \ V \end{bmatrix} = \begin{bmatrix} Net \ rate \ of \ Inflow \\ of \ A \ in \ V \end{bmatrix}$$

"Accumulation Term"   "Convective Term"

We consider two mechanisms by which some substance could enter or exit the control volume: Convection and Dispersion. Convection exits because of flows. This is material transported due to bulk flow. Dispersion occurs even in the absence of flow. It is a process by which the concentration gradient is destroyed.

$$\begin{bmatrix} Rate \ of \ increase \\ of \ A \ in \ V \end{bmatrix} = \begin{bmatrix} Net \ rate \ of \ Inflow \\ of \ A \ in \ V \ due \ to \ convection \end{bmatrix} + \begin{bmatrix} Net \ rate \ of \ Inflow \\ of \ A \ in \ V \ due \ to \ dispersion \end{bmatrix}$$

Accumulation Term

We want to perform a material balance on each of the components that are present. We have Nc components in the system which separates into Np phases.

Let i be the component index, $i = 1, 2, 3, \cdots\cdots\cdots, Nc$

Let j be the phase index, $j = 1, 2, 3, \cdots\cdots\cdots, Np$

Mass balance on a given component:

$$\frac{d}{dt} \int_V \sum_{j=1}^{Np} x_{ij} \, \rho_j \, S_j \, \phi \, dV$$

where, $\rho_j = molar\ density = \dfrac{mass\ density}{Mol.\ wt} = \dfrac{moles}{volume}$

$x_{ij} = mole\ fraction\ of\ component\ i\ in\ phase\ j$

Convection Term

Phase j moves with velocity $\vec{Vj}$ (Darcy velocity determined by kij). Consider the differential are dS.

$\tilde{n} \bullet \vec{V}_j \ dS$:   volumetric flow rate of phase j across dS

$- \ \tilde{n} \bullet \rho_j \ x_{ij} \ \vec{V}_j \ dS$:   moles of i in phase j which flow in through dS

$$\int_S \sum_{j=1}^{Np} - \tilde{n} \bullet \rho_j \ x_{ij} \ \vec{V}_j \, dS$$

Dispersion Term

Dispersion is molecular diffusion in the presence of flow in the presence of a porous medium. We use Fick's law of molecular diffusion and (empirically) modify it to represent dispersion in porous media.

Fick's Law:

$$\vec{J} = - D \nabla C$$

where, D = diffusion coefficient (units: velocity × length)

$$C = \frac{amount}{volume} \text{ (amount: moles, molecular, mass)}$$

$$\vec{J} = \text{diffusion flux}$$

We modify Fick's law for porous media problems:

$$\vec{J}_{ij} = - \phi D_{ij} \nabla\left(\rho_j \, x_{ij}\right)$$

Dispersion Term

$$\int_S \sum_{j=1}^{Np} - \, \tilde{n} \bullet \vec{J}_{ij} \; dS = \int_S \sum_{j=1}^{Np} \tilde{n} \bullet \phi D_{ij} \nabla\left(\rho_j \, x_{ij}\right) dS$$

Putting all the terms together:

$$\frac{d}{dt} \int_V \sum_{j=1}^{Np} \phi \, \rho_j \, x_{ij} \, S_j \; dV = - \int_S \sum_{j=1}^{Np} \tilde{n} \bullet \rho_j \, x_{ij} \, \vec{V}_j \; dS + \int_S \sum_{j=1}^{Np} \tilde{n} \bullet \phi D_{ij} \nabla\left(\rho_j \, x_{ij}\right) dS$$

Applying the divergence theorem

Total divergence within V equals net (out) flux crossing S.

$$\int_{V} \nabla \bullet \ \vec{F} \ dV \ = \ \int_{S} \tilde{n} \ \vec{F} \ dS$$

By applying divergence theorem,

$$\frac{\partial}{\partial t} \sum_{j=1}^{Np} \phi \ \rho_{j} \ x_{ij} \ S_{j} \ + \ \sum_{j=1}^{Np} \nabla \bullet \ \rho_{j} \ x_{ij} \ \vec{V}_{j} \ - \ \sum_{j=1}^{Np} \nabla \bullet \ \phi \ D_{ij} \ \nabla \big(\rho_{j} x_{ij} \big) \ = \ 0 \quad \ldots \ldots \ldots \text{(B.1)}$$

Consider miscible displacement

Assumptions: • There is only one phase. $Np = 1$

   • Binary case (two-component system). $Nc = 2$

   • Flow is one dimensional linear (1-D)

From Eq. B.1

$$\frac{\partial}{\partial t} \big(\phi \ \rho \ x_{i} \big) \ + \ x_{i} \ \rho \ \nabla \bullet \vec{V} \ + \ \vec{V} \bullet \ \nabla \big(x_{i} \ \rho \big) \ - \ \phi \ D_{i} \ \nabla^{2} \big(x_{i} \ \rho \big) \ - \ \nabla \big(x_{i} \ \rho \big) \bullet \nabla \big(\phi \ D_{i} \big) \ = \ 0$$

$i = 1, 2$

Assumptions: • Porosity is constant.

   • Phase velocity, V is constant.

   • Dispersion coefficient is constant.

$$\frac{\partial}{\partial t} \big(\rho \ x_{i} \big) \ + \ \frac{V}{\phi} \ \frac{\partial}{\partial x} \big(\rho \ x_{i} \big) \ - \ D_{i} \ \frac{\partial^{2}}{\partial x^{2}} \big(x_{i} \ \rho \big) \ = \ 0 , \ i = 1, 2$$

Let $\dfrac{V}{\phi} \ = \ u$, $V \ = \ u \ \phi$

$$\frac{\partial}{\partial t}\left(\rho\, x_i\right) + u\,\frac{\partial}{\partial x}\left(\rho\, x_i\right) - D_i\,\frac{\partial^2}{\partial x^2}\left(x_i\, \rho\right) = 0\,,\ i = 1,\,2$$

This is the convection-dispersion equation (CD equation).

Divide through by ρ_i, the molar density of component i,

$$\frac{\partial}{\partial t}\left(\rho\,\frac{x_i}{\rho_i}\right) + u\,\frac{\partial}{\partial x}\left(\rho\,\frac{x_i}{\rho_i}\right) - D_i\,\frac{\partial^2}{\partial x^2}\left(\rho\,\frac{x_i}{\rho_i}\right) = 0$$

where,
$$\rho\,\frac{x_i}{\rho_i} = \frac{\left(\dfrac{moles\ of\ phase\ j}{vol.\ of\ phase\ j}\right)\left(\dfrac{moles\ of\ comp.\ i}{moles\ of\ phase\ j}\right)}{\left(\dfrac{moles\ of\ comp.\ i}{vol.\ of\ comp.\ i}\right)}$$

$$= \frac{vol.\ of\ comp.\ i\ in\ phase\ j}{vol.\ of\ phase\ j} = C_i$$

$$\frac{\partial C}{\partial t} + u\,\frac{\partial C}{\partial x} - D\,\frac{\partial^2 C}{\partial x^2} = 0 \qquad \dots\dots\dots\dots\dots\dots\dots\dots\dots\dots\dots\dots\dots\dots\dots \qquad (B.2)$$

To make the convection-dispersion equation dimensionless, we introduce:

$$x_D = \frac{x}{L}, \qquad\qquad \text{dimensionless distance}$$

where, L is the length of core.

$$t_D = \frac{t}{t^*} = \frac{t\,u}{L}, \qquad \text{dimensionless time}$$

where, u is interstitial velocity $\left(\dfrac{V}{\phi}\right)$

Applying the chain rule to Eq. B.2:

$$\frac{\partial C}{\partial t_D} \frac{\partial t_D}{\partial t} + u \frac{\partial C}{\partial x_D} \frac{\partial x_D}{\partial x} - D \frac{\partial}{\partial x_D} \left(\frac{\partial C}{\partial x_D} \frac{\partial x_D}{\partial x} \right) \frac{\partial x_D}{\partial x} = 0$$

$$\frac{\partial C}{\partial t_D} \left(\frac{u}{L} \right) + \frac{u}{L} \frac{\partial C}{\partial x_D} - \frac{D}{L^2} \frac{\partial^2 C}{\partial x_D^2} = 0$$

$$\frac{\partial C}{\partial t_D} + \frac{\partial C}{\partial x_D} - \frac{D}{Lu} \frac{\partial^2 C}{\partial x_D^2} = 0$$

Let $Pe = \frac{uL}{D}$,   Peclet number

$$\frac{\partial C}{\partial t_D} + \frac{\partial C}{\partial x_D} - \frac{1}{Pe} \frac{\partial^2 C}{\partial x_D^2} = 0 \qquad \dots\dots\dots\dots\dots\dots\dots\dots\dots\dots\dots\dots\dots \quad (B.3)$$

This is the dimensionless form of convection-dispersion equation.

Solution of convection-dispersion equation

Dimensionless convection-dispersion equation

$$\frac{\partial C}{\partial t_D} + \frac{\partial C}{\partial x_D} - \frac{1}{Pe}\frac{\partial^2 C}{\partial x_D^{\,2}} = 0 \qquad \text{...} \qquad \text{(B.3)}$$

Apply initial and boundary conditions,

$$C = 0 \quad at \; t_D = 0, \; 0 < x_D < \infty \qquad \text{.................................} \qquad \text{(B.4)}$$

$$C = 1 \quad at \; x_D = 0 \qquad \text{.................................} \qquad \text{(B.5)}$$

$$t_D > 0$$

$$C \rightarrow 0 \quad at \; x_D \rightarrow \infty \qquad \text{.................................} \qquad \text{(B.6)}$$

Solution procedure

- Convert the PDE into ODE using Laplace Transform.
- Obtain a solution for the transformed ODE.
- Invert the ODE solution to obtain the PDE solution.
- Manipulate the solution for parameter estimation.

The Laplace Transform of C, we will denote as $\bar{C}$:

$$\bar{C} = L\left[C\right] = \int_0^\infty e^{-st} C \, dt \qquad \text{...} \qquad \text{(B.7)}$$

Transform Eq. B.3

$$\left[s\,\bar{C} - C(0) \right] + \frac{\partial \bar{C}}{\partial x_D} - \frac{1}{Pe} \frac{\partial^2 \bar{C}}{\partial x_D^2} = 0 \qquad \dots\dots\dots\dots\dots\dots\dots\dots \quad \text{(B.8)}$$

Applying initial condition (Eq. B.4) into Eq. B.8, C(0) = 0.

Eq. B.8 is a second order ODE with constant coefficients.

Solution:
$$\bar{C} = A\,\exp(mx_D) \qquad \dots\dots\dots\dots\dots\dots\dots\dots\dots\dots\dots \quad \text{(B.9)}$$

$$\frac{d\bar{C}}{dx_D} = Am\,\exp(mx_D) \qquad \dots\dots\dots\dots\dots\dots\dots\dots\dots \quad \text{(B.10)}$$

$$\frac{d^2\bar{C}}{dx_D^2} = Am^2\,\exp(mx_D) \qquad \dots\dots\dots\dots\dots\dots\dots\dots \quad \text{(B.11)}$$

Substitute Eqs. B.9, B.10, and B.11 into ODE Eq. B.8:

$$m^2 - Pe\,m - Pe\,m = 0 \qquad \dots\dots\dots\dots\dots\dots\dots\dots\dots \quad \text{(B.12)}$$

Transform boundary conditions,

$$\bar{C} = \frac{1}{s} \quad at \quad x_D = 0 \qquad \dots\dots\dots\dots\dots\dots\dots\dots\dots \quad \text{(B.13)}$$

$$\bar{C} \rightarrow 0 \quad as \quad x_D \rightarrow \infty \qquad \dots\dots\dots\dots\dots\dots\dots\dots \quad \text{(B.14)}$$

From Eq. B.12,

$$m = \frac{Pe \pm \sqrt{Pe^2 + 4\,Pe\,s}}{2}$$ ………………………………….... (B.15)

Substitute Eq. B.15 into Eq. B.9

$$\bar{C} = A\exp\left[\frac{Pe \pm \sqrt{Pe^2 + 4\,Pe\,s}}{2}\,x_D\right]$$ …………………….. (B.16)

where, $\sqrt{Pe^2 + 4\,Pe\,s} > Pe$

We choose the negative root to satisfy B.C. (Eq. B.14).

$$\bar{C} = A\exp\left[\frac{Pe - \sqrt{Pe^2 + 4\,Pe\,s}}{2}\,x_D\right]$$ …………………….. (B.17)

$A = \dfrac{1}{s}$, since $\bar{C} = \dfrac{1}{s}$ at $x_D = 0$

Therefore, $\bar{C} = \dfrac{1}{s}\exp\left[\dfrac{Pe - \sqrt{Pe^2 + 4\,Pe\,s}}{2}\,x_D\right]$ ………………… (B.18)

To invert Eq. B.18, we will define a shifted Laplace variable.

Let $P = s + \dfrac{Pe}{4}$ …………………………………………………….... (B.19)

where, P is a shifted Laplace transform variable.

Substitute Eq. B.19 into Eq. B.18,

$$\bar{C} = \frac{1}{P - \frac{Pe}{4}} \exp\left(\frac{Pe\ x_D}{2}\right) \exp\left(-x_D\ \sqrt{Pe\ P}\right) \quad \dots\dots\dots\dots \quad (B.20)$$

Comparing Eq. B.20 with a table of Laplace transforms.[36]

$$f(P) = \frac{e^{-qx}}{P - \alpha} \ ; \ q = \sqrt{\frac{P}{k}} \quad \dots\dots\dots\dots\dots\dots\dots\dots\dots\dots \quad (B.21)$$

$$\left.\begin{array}{l} \alpha = \dfrac{Pe}{4} \\[2ex] x = x_D \\[2ex] k = \dfrac{1}{Pe} \end{array}\right\} \quad \dots\dots\dots\dots\dots\dots\dots\dots\dots\dots\dots\dots \quad (B.22)$$

$$C = \frac{1}{2} \exp\left(\frac{Pe\ \tilde{t}}{4}\right) \left\{erfc\left[\frac{x_D - \tilde{t}}{2\sqrt{\tilde{t}/Pe}}\right]\right\} + \exp(Pe\ x_D)\ erfc\left[\frac{x_D + \tilde{t}}{2\sqrt{\tilde{t}/Pe}}\right]$$

$$= F\left(\tilde{t}\right) \quad \dots\dots\dots\dots\dots\dots\dots\dots\dots\dots\dots\dots\dots\dots\dots\dots\dots \quad (B.23)$$

To obtain $F(t_D)$, we use the shifting property of the Laplace transform.

$$L^{-1}\left[f\left(s + \frac{Pe}{4}\right)\right] = L^{-1}\left[f\left(s - \left(\frac{-Pe}{4}\right)\right)\right] = L^{-1}\left[f(s - a)\right] ; \quad a = -\frac{Pe}{4}$$

$$= \exp^{-\frac{Pe}{4}\tilde{t}} F\left(\tilde{t}\right) = F(t_D)$$

$$C = \frac{1}{2}\left\{erfc\left[\frac{x_D - t_D}{2\sqrt{t_D/Pe}}\right] + e^{Pe\ x_D}erfc\left[\frac{x_D + t_D}{2\sqrt{t_D/Pe}}\right]\right\} \quad .... \quad (B.24)$$

This is the solution of dimensionless convection-dispersion equation.

VITA

Name:	Jeong Gyu Seo
Date of Birth:	June 1, 1970
Place of Birth:	Seoul, Korea
Parents:	Soobeom Seo Dongsil Cho
Permanent Address:	Taeyoung Apt. 1701-1305 Hoogokmaul Ilsan3 dong Ilsan gu Goyang si Kyounggi do 411-737, Korea.
Education:	B.S., Petroleum Engineering (Feb. 1997) Hanyang University, Seoul, Korea. M.S., Petroleum Engineering (Feb. 1999) Hanyang University, Seoul, Korea. Ph.D., Petroleum Engineering (May 2004) Texas A&M University, College Station, Texas, USA.
Professional Affiliations:	Society of Petroleum Engineers, Member.